Runoff Dynamics and Its Regime Changes in the Major River Basins of Africa From GRACE and GRACE-FO Observations

Ayman M. Elameen, Shuanggen Jin, *Senior Member, IEEE*, and Isaac Sarfo

***Abstract*—The major African basins supply freshwater to around 0.5 billion people, while monitoring runoff fluctuations in these basins is still challenging due to limited in-situ data and high costs. Hydrologic models are widely used for this purpose, but they have certain drawbacks with larger uncertainty and low accuracy in poorly gauged basins. This study attempts to address this issue by using Gravity Recovery and Climate Experiment (GRACE)/GRACE Follow-On (GRACE-FO) satellite measurements and remote sensing data to estimate runoff changes in five major African basins from 2003 to 2019. Moreover, a comprehensive framework was developed to quantify interannual and intraannual runoff regimes and their changes from the perspectives of magnitude, variability, and duration. Results showed that runoff changes estimated from GRACE/GRACE-FO in the major African basins were in good alignment with those from the Global Land Data Assimilation System, European Centre for Medium-Range Weather Forecasts Reanalysis 5, and Soil Conservation Service-Curve Number. Seasonal runoff increased in the Nile (0.12 to 0.46 mm/a, $p < 0.05$) and Congo (0.52 to 0.76 mm/a, $p < 0.05$) basins during 2003–2019, while it was decreased in the Zambezi (–1 to –0.34 mm/a, $p < 0.05$) and Orange (–0.54 to –0.24 mm/a, $p < 0.05$) basins during the same period. Further in-depth analysis showed that the impacts of climate change in the study area were the primary contributors to changes in runoff. Monthly runoff in the Nile, Congo, and Niger basins showed an increase in magnitude, duration, and variability. In contrast, the Zambezi and Orange basins experienced a decrease in runoff magnitude, along with reduced variability and duration. In addition, large-scale atmospheric circulations, such as El-Nino Southern Oscillation Index and Indian Ocean Dipole, have been found to be associated with changes in runoff within the study area, as demonstrated by correlation and wavelet analysis. Our findings provided valuable insights into long-term runoff changes in major African basins and enhanced the understanding of hydrologic processes in poorly gauged regions.**

***Index Terms*—Africa, climate change, gravity recovery and climate experiment (GRACE)/GRACE follow-on (GRACE-FO), major river basins, runoff.**

I. Introduction

IT is well recognized that river basins play an essential role in supporting societal and economic development, particularly concerning water stability and scarcity in Africa. Recent studies have pointed out the impacts of climate change and increasing population on world's river basins [1], [2]. Thus, it is necessary to measure and evaluate the water cycle state of basins, specifically in regions with alarming hydrologic conditions, to ensure freshwater supply, regulate water quality and quantity, and mitigate hazards associated with climate changes (e.g., floods and droughts). Runoff, as one of most fundamental and dynamic parameters of the water cycle, has a determining role in the regional hydrologic system by shaping the availability and distribution of water resources. Hence, it is important to understand the fluctuations in runoff and underlying causes under the changing environment for better water resources management [3], [4], [5].

Conventionally, variations in the runoff level are estimated using in-situ monitoring stations [6]. However, in many African regions, long-term runoff records remain challenging due to inadequate hydrometeorological infrastructure and financial constraints [7]. This jeopardizes the grasping of hydrologic processes and water resources management over these regions. Nowadays, there has been increasing global runoff estimates derived from different models, such as the Global Land Data Assimilation System (GLDAS) [8], the WaterGAP model [9], and the Famine Early Warning Systems Network Land Data Assimilation System [10]. Although these techniques provide a unique opportunity for large-scale monitoring of runoff, they have significant uncertainties in regions with insufficient field observations [11]. As a result, this may limit their applicability in poorly gauged African basins. On the other hand, creating a physical-based model (e.g., Soil and Water Assessment Tool), particularly over a large spatial extent, demands huge sets of information, complex parameterization, greater computational capability, and validation process against in-situ records, which is limited or discontinuous due to missing data [6]. Therefore, it is important to employ alternative approaches such as remote

Received 18 October 2024; revised 15 May 2025 and 22 July 2025; accepted 18 August 2025. Date of publication 22 August 2025; date of current version 16 September 2025. This work was supported by the Henan International Science and Technology Cooperation Key Program under Grant 241111520700. *(Corresponding author: Shuanggen Jin.)*

Ayman M. Elameen is with the School of Remote Sensing and Geomatics Engineering, Nanjing University of Information Science and Technology, Nanjing 210044, China, and also with the Organization of African Academic Doctors, Nairobi 00100, Kenya.

Shuanggen Jin is with the School of Remote Sensing and Geomatics Engineering, Nanjing University of Information Science and Technology, Nanjing 210044, China, also with the School of Artificial Intelligence, Anhui University, Hefei 230601, China, and also with the School of Surveying and Land Information Engineering, Henan Polytechnic University, Jiaozuo 454003, China (e-mail: sgjin@hpu.edu.cn).

Isaac Sarfo is with the College of Geography and Environmental Science, Henan University, Kaifeng 475004, China, and also with the Organization of African Academic Doctors, Nairobi 00100, Kenya.

Digital Object Identifier 10.1109/JSTARS.2025.3601672

sensing techniques, which can offer accurate information on the variations in runoff.

Since the mission of Gravity Recovery and Climate Experiment (GRACE) and GRACE Follow-On (GRACE-FO) satellites have been launched [12], [13], significant estimates on the variations in total water storage (TWS) with global coverage have been supplied to hydrologists and researchers [14], [15], [16]. These satellites can determine fluctuations in the gravity field and directly offer mass redistribution and variations in the volume of water resources [16], [17], including surface water, soil moisture, groundwater, snow, and glaciers over a wide extent [13]. Numerous studies have been conducted for different purposes utilizing the information derived from the GRACE and GRACE-FO satellites, for example, estimation of TWS [18], [19], [20], [21], groundwater storage change assessment [12], [22], [23], [24], monitoring drought and flood [25], [26], [27], tracking glacier and snow melting [28], [29], [30], [31], calculating evapotranspiration (ET) [32], [33], [34], [35], and surveying and navigating investigations [36], [37], [38], [39].

One of the most significant and practical capabilities of GRACE/GRACE-FO satellites datasets is the estimation of runoff. So far, numerous works worldwide [6], [40], [41], [42], [43], [44], [45], [46] have reported to estimate and evaluate variations in runoff. Despite its great importance of monitoring the variability of a river's runoff and developing a sustainable management plan in Africa with critical water resource situations, limited studies have concentrated on the estimation of runoff fluctuations using GRACE/GRACE-FO datasets [47], [48].

Although several remote sensing tools exist for runoff estimation, including precipitation (Prec) missions [e.g., tropical rainfall measuring mission (TRMM) and global precipitation measurement (GPM)], ET products (e.g., moderate resolution imaging spectroradiometer (MODIS) and Landsat), soil moisture datasets [e.g., soil moisture active passive (SMAP) and soil moisture and ocean salinity (SMOS)], and river altimetry missions [e.g., surface water and ocean topography (SWOT) and Jason series] [49], [50], [51], [52], these platforms primarily provide surface-based observations. As a result, they require integration through complex hydrological models to infer runoff, often introducing substantial uncertainty, particularly regarding subsurface contributions. In contrast, GRACE and GRACE-FO offer a unique advantage by directly measuring changes in terrestrial water storage (TWS), encompassing all water compartments [53], including surface water, soil moisture, groundwater, snow, and ice. This integrated perspective enables a more physically consistent estimation of runoff via the water balance approach. Unlike traditional remote sensing products, GRACE observations are unaffected by vegetation cover, atmospheric variability, or land surface heterogeneity, making them especially useful in data-scarce and groundwater-dependent basins. While the spatial resolution of GRACE is coarser than other satellite products, its ability to capture both surface and subsurface hydrological changes makes it a uniquely powerful and reliable tool for large-scale runoff assessments.

Changes in runoff have affected freshwater ecosystems and food diversity globally [3], [49], [54]. As such, several studies conducted over Africa in recent decades have focused on temporal and spatial changes of runoff. For example, in the Nile basin, Gebremicael et al. [55] and Abebe et al. [56] quantified runoff changes in the Blue Nile subbasin using field observations for the periods 1971–2009 and 1984–2014, respectively. Both studies reported increasing runoff trends, largely attributed to shifts in climate. Similarly, Dinka and Klik [57] applied the Soil Conservation Service-Curve Number (SCS-CN) hydrological model in the Lake Basaka catchment (Upper Blue Nile basin), finding a statistically significant increase in runoff from 1973 to 2007. In the Congo basin, runoff remains relatively stable due to dense rainforest cover [58], although deforestation is expected to affect long-term runoff dynamics [59], [60]. In the Niger basin, Mahé and Paturel [61] examined runoff variability across the Sahelian zone using in-situ gauge data (1970–2006), identifying a sharp decline during the 1970s–1980s drought period, followed by partial recovery from the 1990s onward. Efon et al. [62] analyzed European Centre for Medium-Range Weather Forecasts Reanalysis 5 (ERA5) data spanning 41 years and observed overall decreasing trends in both annual and seasonal runoff across West Africa, including the Niger basin. Future projections suggest increased runoff in the upper Niger basin but a continued decline in the Sahelian zone [63]. In the Zambezi basin, studies revealed spatially heterogeneous trends—both increasing and decreasing—primarily influenced by climate variability and hydraulic infrastructure development [63], [64], [65]. Most assessments in the Orange basin report declining runoff, driven by both climate change and anthropogenic activities such as irrigation and industrial water abstraction [66], [67]. In North Africa, Achite et al. [68] used hydrological station data from 1973 to 2012 to identify decreasing runoff trends in the Wadi Mina basin in northwestern Algeria. Similarly, in the Lake Chad basin, Mahmood and Jia [69] combined hydrologic engineering center-hydrologic modeling system (HEC-HMS) modeling with in-situ data and found a substantial decline in annual runoff from 1951 to 2013. Regional studies such as those mentioned earlier were mainly concentrated on the change rate to analyze the variations in runoff. However, this may not lead to a sufficient understanding of the overall variations in the runoff conditions. The alterations in the runoff regime can be analyzed using various indicators [70], [71], [72], [73] and reflected in different dimensions, including magnitude, frequency, duration, timing, and rate of change [74], [75], [76], [77], [78], [79], [80]. However, the understanding of runoff dynamics and regime shifts remains limited across Africa's major river basins, largely due to data constraints and insufficient basin-scale analyses.

Investigating the relationship between changes in runoff and their potential driving factors has become a prominent area of research in recent years. Typically, the drivers of runoff variability include both regional and global environmental factors [81], [82]. The regional environmental factors encompass climatic variables (Prec, temperature (Temp), and potential ET) [4], vegetation [83], and human activities [84]. The global environmental factors refer to large-scale atmospheric circulations [85], such as El-Nino Southern Oscillation Index (ENSO) and Indian Ocean Dipole (IOD) [86]. While the interactions between runoff and regional environmental factors have been relatively well

TABLE I
AREA, LENGTH, CLIMATE, AND MEAN ELEVATION OF BASINS CONSIDERED IN THIS STUDY

River basin	Area (10^5 km^2)	Length (Km)	Climate	Elevation (m)
Nile	31.8	6700	Semiarid	726
Congo	37.5	4667	Humid	737
Niger	21.8	4200	Semiarid	419
Zambezi	13.8	2650	Semiarid	1003
Orange	9.7	2300	Semiarid	270

investigated [69], [87], [88], very few investigations have documented the teleconnection between global atmospheric circulations and runoff in Africa [86], [89]. Most of the existing studies dwelt on regions with hydrological datasets that are sufficiently long and complete. In areas where data are scarce and variability is high, understanding the global climatic teleconnections that drive runoff variability can be limited. However, recent advancements in remote sensing technology, such as the capabilities of GRACE/GRACE-FO satellites to provide accurate runoff estimates over large areas, can help address this issue. This approach will enhance our understanding of the relationship between global atmospheric circulations and runoff variability in regions with limited data. Furthermore, early studies were mainly focused on certain timescales (e.g., interannual) to analyze the effect of large-scale atmospheric circulations on runoff. According to Li et al. [90], investigating the relationship between controlling factors and runoff at various timescales can provide a clearer explanation of how these factors influence changes in runoff. Therefore, it is essential to examine the impact of global climate teleconnections on runoff across multiple scales to gain a deeper understanding of the mechanisms driving runoff variability.

In recognition of the research progress, gaps, and opportunities expatiated earlier, this study utilized GRACE/GRACE-FO satellites observations to estimate long-sequence runoff changes in Africa's five major river basins (i.e., Nile, Congo, Niger, Zambezi, and Orange) from January 2003 to December 2019. The variations are characterized in seasonal runoff, and the responses with climate factors were analyzed in depth. Furthermore, we proposed a statistical framework to quantify the alterations in the runoff regime from the aspects of magnitude, variability, and duration, in which both inter- and intraannual runoff regimes and their changes were analyzed and investigated. In addition, considering the role of global climate teleconnections in runoff variability, the coupling relationships between runoff and the climate teleconnection modes were examined at different timescales using Pearson correlation and wavelet coherence analysis.

II. STUDY AREAS AND DATA

A. Description of the Study Domain

Africa is the second-largest continent in the world, encompassing an area of approximately 30 million km^2. It is also the second most populous continent, with a population of around 1.5 billion people [91]. It contains 63 transboundary river basins that cover about 64% of its land mass and also home to around 77% of Africa's population [92]. This study focuses on Africa's five major river basins: the Nile River Basin (NRB), Congo River Basin (CRB), Niger River Basin (NIRB), Zambezi River Basin (ZRB), and Orange River Basin (ORB) (see Fig. 1). These basins represent the major sources of temporal variations of hydrological masses throughout the continent. They lie between 32.6°S to 31.4°N and 11.5°W to 39.8°E and cover a broad range of different sizes and climate zones. Further details regarding these basins are provided in Table I.

B. Prec Data

In this study, we obtained the Prec dataset (2003–2019) from the TRMM [50]. This dataset has found extensive application in hydrological, meteorological, and ecological studies, especially in regions with limited availability of ground-based Prec measurements [93], [26]. The level 3 monthly gridded data product (TRMM-3B43), with a 0.25° × 0.25° spatial resolution, was utilized in this study. The data can be accessed online.[1]

C. ET Data

We collected the monthly ET dataset from the Global Land Evapotranspiration Amsterdam model (GLEAM). The GLEAM estimates different components of land ET using the Priestley–Taylor equation [94]. The primary variables involve air Temp, land surface temperature (LST), Prec, soil moisture, vegetation optical depth, and snow water equivalent [95]. The recent version of GLEAM v4.1a at a spatial resolution of 0.25° was utilized in this study, and the data were acquired online.[2] Remote-sensing-based ET data from the MODIS were also used in this study. The MODIS ET data are retrieved from the Penman–Monteith formula based on daily reanalysis meteorological data (air pressure, air Temp, humidity, and radiation) [96]. Here, the MOD16A2 ET product, with a spatial resolution of 500 m and a temporal resolution of eight days, was used over the period 2003–2019. The eight-day ET data were averagely weighted to obtain the monthly ET values. The data are freely available online.[3]

[1][Online]. Available: http://trmm.gsfc.nasa.gov/data_dir/data.html
[2][Online]. Available: https://www.gleam.eu/
[3][Online]. Available: https://modis.gsfc.nasa.gov/data/dataprod/mod16.php

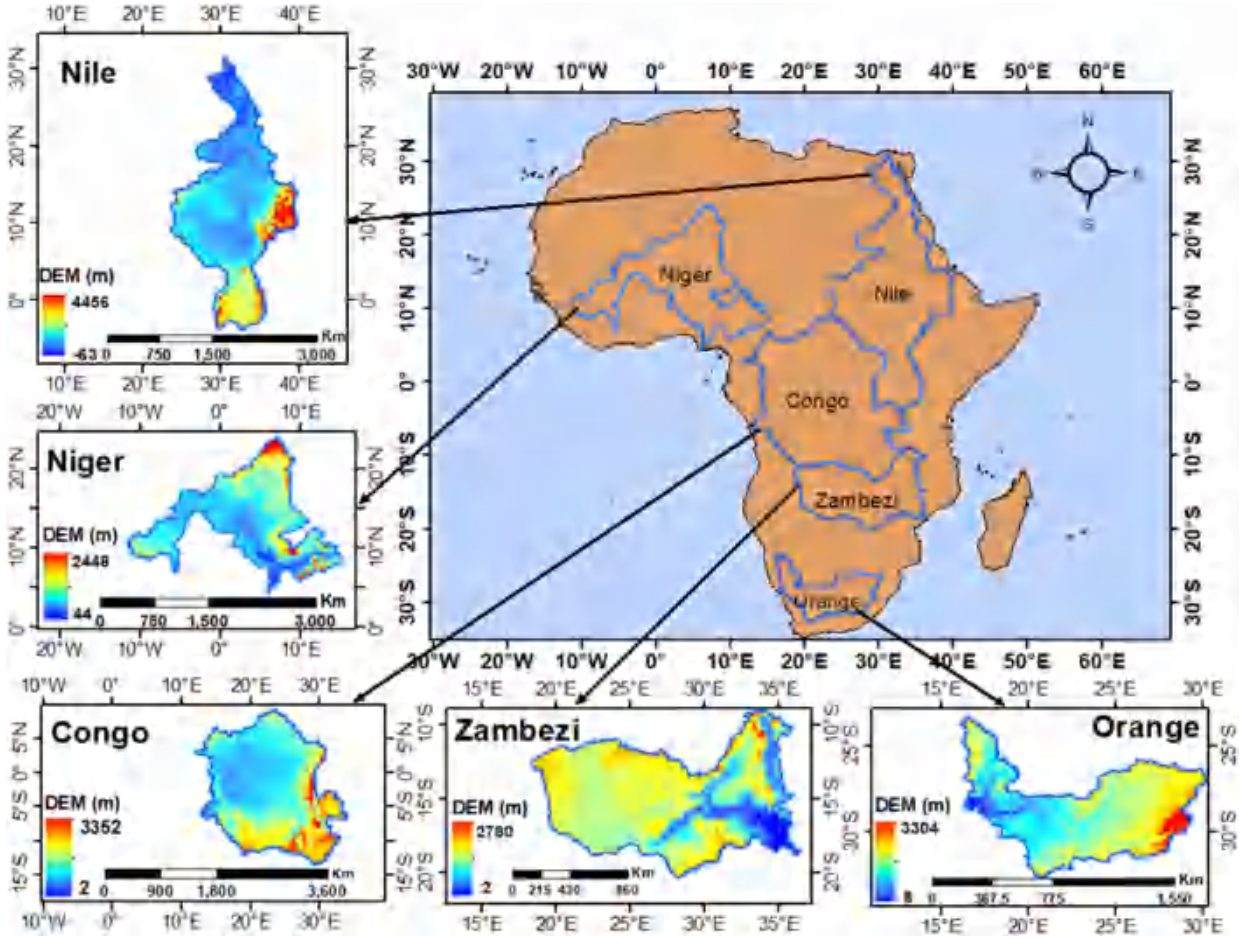

Fig. 1. Location of river basins selected in this study and the elevations along the basins.

D. Runoff Data

This article used the runoff dataset from the GLDAS-2.1 [8] model for comparison and analysis. The GLDAS is jointly developed by NASA's Goddard Space Flight Center and the National Center for Environmental Prediction. The product is obtained utilizing a land surface model (LSM) and data assimilation technology driven by satellite and ground observation data [34]. GLDAS-2.1 consists of three models: NOAH, Variable Infiltration Capacity (VIC), and Community Land Model (CLM) [97]. For this study, we used 1° monthly runoff from the aforementioned three models during the period of 2003–2019. The data can be accessed online.[4] A reanalysis-based runoff dataset from the ERA5 [98] was also utilized in this study. The ERA5 replaced ERA-Interim on 31 August 2019. Its dataset includes extensive historical data, along with global estimates produced using advanced modeling and data assimilation systems [62]. This study selected monthly gridded runoff data with a spatial resolution of 0.25° from 2003 to 2019. The data are freely available online. [5]

E. GRACE and GRACE-FO Observations

The GRACE mission (April 2002 to June 2017) and its successor, GRACE-FO (June 2018 to present), were established by NASA and the German Aerospace Center to monitor the earth's gravity field. These data are valuable for studying changes in TWS across both land and oceans [99]. To date, the datasets of GRACE/GRACE-FO satellites are mainly obtained from the Center for Space Research (CSR), the German Research Center, and the Jet Propulsion Laboratory [100]. The estimation methods for TWS based on GRACE and GRACE-FO can be categorized into two groups, depending on different inversion concepts: the spherical harmonic coefficient (SHC) method and the mass concentration model [101]. In this study, we selected the sixth release of the SHC solution processed by the CSR to derive gridded terrestrial water storage anomaly (TWSA) data from 2003 to 2019, employing a spatial resolution of 1°. The data can be accessed online.[6]

F. Data for LST

The LST data used in this study were obtained from MODIS [102]. These data are produced by two satellites: Terra

[4][Online]. Available: https://hydro1.gesdisc.eosdis.nasa.gov/data/GLDAS

[5][Online]. Available: https://www.ecmwf.int/en/forecasts/datasets/reanalysis-datasets/era5

[6][Online]. Available: https://www2.csr.utexas.edu/grace

(MOD11C3) and Aqua (MYD11C3), which were launched in 1999 and 2002, respectively. Terra crosses the equator at 10:30 and 22:30, moving from north to south, while Aqua crosses at 13:30 and 1:30, traveling from south to north [103]. Monthly data (MOD11C3/MYD11C3) from the Terra and Aqua satellites between 2003 and 2019 were utilized in this study. The data possess a spatial resolution of 0.5° × 0.5° and are available online.[7]

G. Curve Number (CN) Data

The CN is a key component of the SCS-CN model [104]. It is a dimensionless value that represents the conversion of rainfall into runoff. CN values range from 0 to 100, with higher values indicating a larger percentage of rainfall that is converted into runoff [105]. The present study used a gridded CN dataset from the GCN250 product [106]. The GCN250 data are generated from the combination of European Space Agency Climate Change Initiative Land Cover Project maps and hydrologic soil group data of the HYSOGs250m product. The data have a spatial resolution of 250 m and are available online.[8]

H. Teleconnection Indices

Monthly teleconnection indices, namely, ENSO and IOD, were employed in this study to investigate their relationships with runoff variabilities during 2003–2019. The ENSO[9] and IOD[10] data were acquired online.

III. Methods

A. Terrestrial Water Storage Change (TWSC) Estimation From GRACE/GRACE-FO

GRACE/GRACE-FO SHC time series are converted to monthly grid equivalent water height (EWH) or TWSA using the following formula [107]:

$$\mathrm{EWH}(\theta,\lambda) = \frac{a\,\rho_{\mathrm{ave}}}{3\,\rho_{\mathrm{water}}} \sum_{l=0}^{\infty} \sum_{m=0}^{l} \bar{P}_{lm}(\cos\theta) \frac{2l+1}{1+K_l} \left(\Delta\bar{C}_{lm}\cos(m\lambda) + \Delta\bar{S}_{lm}\sin(m\lambda)\right) \quad (1)$$

where a represents the mean radius of the earth (6378 km), θ is the colatitude, λ is the longitude, ρ_{ave} is the mean density of the earth (5517 kg/m^3), ρ_{water} is the density of water (1000 kg/m^3), l and m correspond to the order and the degree of SHCs, respectively, $\bar{P}_{lm}(\cos\theta)$ denotes the normalized Legendre function, K_l is the loading love number, and $\Delta\bar{C}_{lm}$ and $\Delta\bar{S}_{lm}$ are the SHC anomalies provided by GRACE and GRACE-FO.

A number of process procedures are applied to the SHC solution as follows. First, C_{1} coefficients are replaced by estimates from the atmosphere and ocean models [108], C_{20} coefficients are replaced by solutions from satellite laser ranging [109], and glacial isostatic adjustment [110] is applied to the solution. Second, a 300-km-wide Gaussian filter was applied to the SHCs [111] with a maximum degree/order of 60, and the decorrelation filter is used to reduce the correlated errors in GRACE/GRACE-FO data [112]. Thereafter, the leakage reduction and averaging approach suggested by Khaki et al. [113] is utilized to minimize the leakage error contributions over the targeted river basins. Finally, the 18 missing months (from January 2003 to June 2017) in GRACE time series and 11 consecutive months' data gaps (from July 2017 to May 2018) represent the gaps among GRACE ending and GRACE-FO launching periods; in addition, two missing months in GRACE-FO data (August and September in 2018) are filled using the singular spectrum analysis (SSA) gap-filling method [114]. Specifically, we applied a two-step SSA approach. Short gaps within GRACE (SSA-filling-a) were filled using a fixed window length ($M = 24$) and 12 retained components ($K = 12$), which effectively preserved the signal. For the longer 11-month gap between missions and smaller gaps in GRACE-FO (SSA-filling-b), we used cross validation to select optimal M (12–72 months) and K (1–12) values for each SHC by minimizing root-mean-square error. This method ensured accurate reconstruction of both short- and long-term variability. MATLAB script is employed for the imputation process.

In each basin, monthly TWSC is estimated from GRACE/GRACE-FO monthly TWSA series using the second-order central differencing function as follows [6]:

$$\mathrm{TWSC} = \frac{dS}{dt} = \frac{d(\mathrm{TWSA})}{dt} = \frac{\mathrm{TWSA}(t+1) - \mathrm{TWSA}(t-1)}{2\Delta t} \quad (2)$$

where TWSC is the terrestrial water storage change for month, TWSA (t + 1) and TWSA (t – 1) are terrestrial water storage anomaly for months t + 1 and t – 1, respectively, and the time period Δt is taken as one month in the research.

B. Runoff Estimation From GRACE/GRACE-FO and Water Balance Method

In a certain region or watershed, the water balance equation utilizing GRACE/GRACE-FO data can be arranged as follows [41]:

$$\frac{d(\mathrm{TWSA})}{dt} = \frac{dS}{dt} = \mathrm{Prec} - \mathrm{ET} - R \quad (3)$$

where $\frac{dS}{dt}$ represents the change in TWS (mm), Prec is precipitation (mm), ET is evapotranspiration (mm), and R is the total runoff (mm). By rearranging the aforementioned equation, the total runoff in our study can be calculated as follows [6]:

$$R = \mathrm{Prec} - \mathrm{ET} - \frac{dS}{dt}. \quad (4)$$

Herein, $\frac{dS}{dt}$ was directly derived from GRACE/GRACE-FO datasets, as depicted in (2), the Prec data were provided by the TRMM, and the ET data were collected from MODIS and GLEAM products. We resampled the TRMM Prec, MODIS, and GLEAM grids to match the resolution of the TWSA grid, ensuring compatibility in spatial scales across all datasets.

[7][Online]. Available: https://modis.gsfc.nasa.gov/data/

[8][Online]. Available: https://figshare.com/articles/dataset/GCN250_global_curve_number_datasets_for_hydrologic_modeling_and_design/7756202

[9][Online]. Available: http://psl.noaa.gov/data/

[10][Online]. Available: http://www.jamstec.go.jp/frcgc/research/d1/iod/DATA/dmi

C. SCS-CN Model

The SCS-CN is a commonly used approach for determining runoff depth from a rain event and the characteristics of the watershed in which it occurs [115]. The technique is relatively simple to apply, demands less information, and is quite accurate [104]. The runoff depth is computed with the SCS-CN as follows [116]:

$$R = \frac{(\text{Prec} - 0.2S)^2}{\text{Prec} - 0.8S} \tag{5}$$

where R is the direct runoff, Prec is the precipitation, and S is the potential maximum retention.

S can be calculated as follows:

$$S = \frac{25400}{\text{CN}} - 254 \tag{6}$$

$$\text{CN} = \frac{\sum A_i \text{CN}_i}{\sum A_i} \tag{7}$$

where CN_i is the curve number for a particular domain and A_i is the area of the domain.

In this study, TRMM Prec and GCN250 CN data are employed to estimate runoff depth from the SCS-CN method.

D. Time-Series Decomposition

This study implements the Seasonal-Trend decomposition procedure based on LOESS (STL) approach to decompose the original time series of the runoff into long-term, seasonal, and residual signals. The method was suggested by Cleveland et al. [117] and formulated as follows:

$$X_T = X_L + X_S + X_R \tag{8}$$

where X_T, X_L, X_S, and X_R represent the original time-series, long-term, seasonal, and residual variability, respectively. In this study, we only focus on the long-term trends in the runoff time series that appear after applying the STL method on a monthly timescale.

E. Mutation Point Identification

The detection of the abrupt mutation points in the time series of runoff is done using the nonparametric Pettitt's test [118]. This test is less sensitive to outliers and biases in data in comparison to other methods [119] and has been utilized in several prior hydrological studies [3], [120]. For a certain series V ($v_1, v_2, \ldots, v_n$), it can be split into two series $v_1, v_2, \ldots, v_t$ and $v_{t+1}, v_{t+2}, \ldots, v_n$ based on the mutation point. The test statistic $W_{t,n}$ is expressed as follows:

$$W_{t,n} = \sum_{i=1}^{t} \sum_{j=1}^{n} \text{sgn}\,(v_t - v_j), \quad \text{if } t = 2, \ldots, n \tag{9}$$

where sgn () is a sign function with values of -1, 0, or + 1. The mutation point is defined as follows, where $|W_{t,n}|$ reaches the maximum:

$$Q_n = \text{Max}\,|W_{t,n}|\,. \tag{10}$$

The level of significance of Q_n is identified when the ρ-value is less than 0.05. The series is separated into two subseries at the place where the mutation point occurs.

F. Trend Analysis

This study utilized Sen's slope estimator (SS) to estimate the rate of change in runoff time series and the modified Mann–Kendall (MMK) test to determine the statistical significance of the changes observed. These methods have been widely employed in the literature [121], [122]. The MMK test is considered to be more accurate and adaptive compared to the original Mann–Kendall test in identifying changes in hydroclimatological time series [123]. The MMK test is less likely to incorrectly detect a trend in autocorrelated records [124]. The details regarding the MMK test and Sen's SS analysis can be found in [125].

G. Framework for Assessing the Runoff Regime Alterations

Indicatively, we developed a framework to examine changes in the runoff regime and to understand how climate change affects the hydrological system in understudied basins. The proposed framework is analogous to the one utilized in [72] and [119] for evaluating water storage and flow regimes, in which both inter- and intraannual regimes were quantified. The method includes various hydrological metrics (see Table II) that can be categorized into three groups: magnitude, variability, and duration. The differences in metric values between the pre- and postmutation periods can be regarded as the effects of climate change. This overall process is summarized in Fig. 2.

The absolute difference in average (MMR50), low (LMR25), and high monthly runoff (HMR75) between premutation period and postmutation period (see Table II) is utilized to evaluate the magnitude change across the studied basins. In addition, we utilized standard deviation (STD) and range (maximum–minimum) to characterize the intraannual variability of runoff. Higher variability indicates a more unstable hydrological system, and vice versa [72]. To demonstrate changes in variability, we use the relative differences in range and STD between the premutation and postmutation periods (see Table II). In addition, we illustrate the duration change in runoff storage by examining the absolute difference in the time of exceeding median runoff storage (DMR) between these two periods.

H. Pearson's Correlation Coefficient (r)

The Pearson correlation coefficient (r) depicts the degree of linear connection that exists between two time series X and Y [126]. If r in the following equation is equal to 1, then both time series have a perfect positive relation; if r is equal to zero, then the variables do not have any relation:

$$r = \frac{\sum_{i=1}^{n} \left(X - \bar{X}\right)\left(Y - \bar{Y}\right)}{\sqrt{\sum_{i=1}^{n} \left(X - \bar{X}\right)^2} \sqrt{\sum_{i=1}^{n} \left(Y - \bar{Y}\right)^2}} \tag{11}$$

where n denotes the number of samples, $\bar{X}$ marks the mean value of variable X, and $\bar{Y}$ connotes the mean value of variable Y.

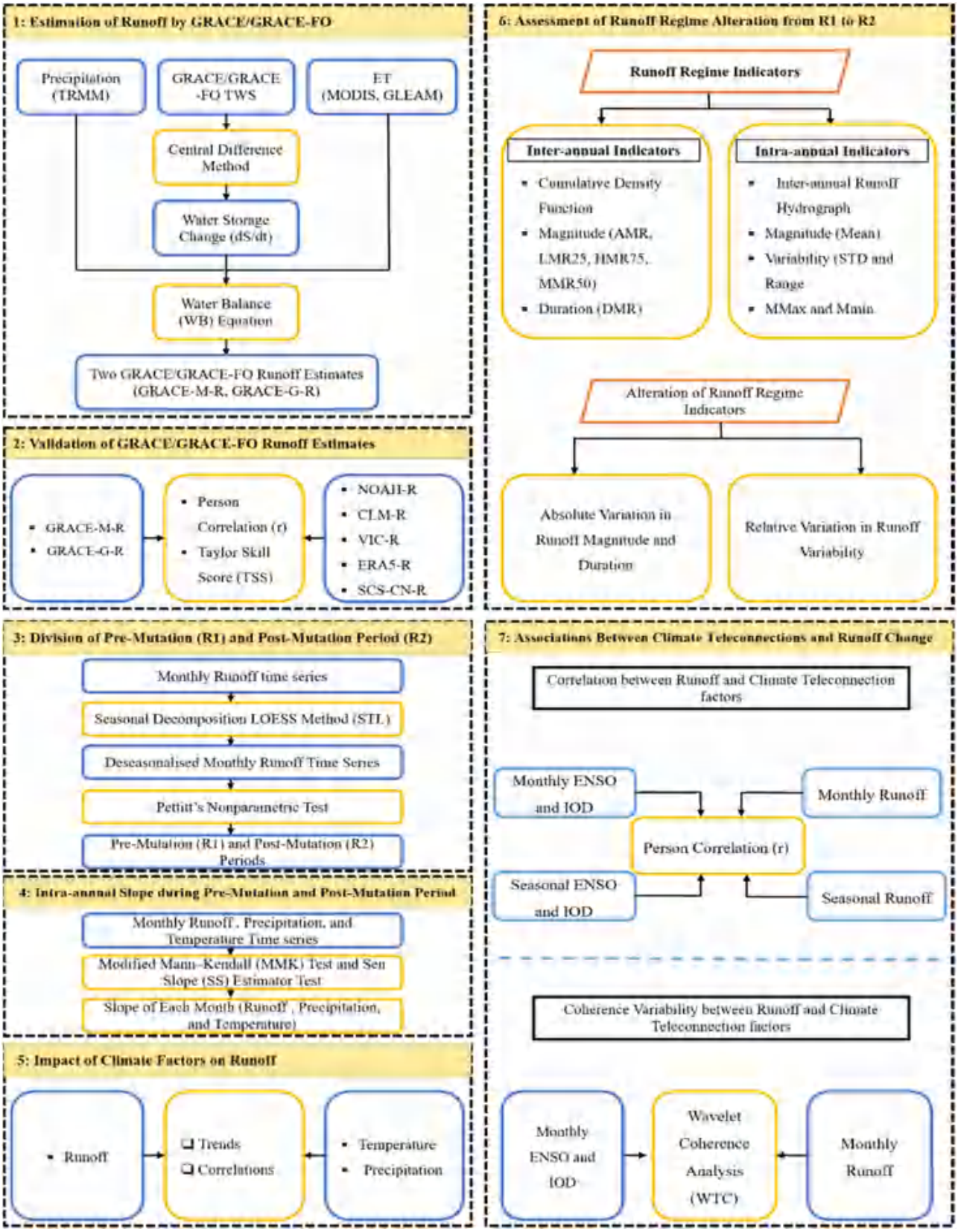

Fig. 2. Flowchart of analysis and process for this study.

TABLE II
HYDROLOGICAL INDICATORS OF RUNOFF REGIME CHANGE

No.	Characteristics	Runoff regimes	Hydrological metrics	Abbreviation	Alteration
1	Magnitude	Monthly runoff	Average monthly runoff	AMR	$AMR_2 - AMR_1$
2		Monthly runoff	Low monthly runoff (25th percentile)	LMR25	$LMR25_2 - LMR25_1$
3		Monthly runoff	High monthly runoff (75th percentile)	HMR75	$HMR75_2 - HMR75_1$
4		Monthly runoff	Median monthly runoff (50th percentile)	MMR50	$MMR50_2 - MMR50_1$
5	Variability	Average runoff	Standard deviation of monthly mean runoff	STD	$(STD_2 - STD_1)/STD_1$
6		Average runoff	Difference between maximum and minmum of monthly mean runoff	Range	$(Range_2 - Range_1)/Range_1$
7	Duration	Median runoff	Time exceeding of median runoff	DMR	$DMR_2 - DMR_1$

Subscripts 1 and 2 refer to the premutation period and postmutation period, respectively.

I. Taylor Skill Score (TSS)

The TSS is an effective approach for determining how closely two sets of information are related to one another [127]. The value of TSS varies between 0 and 1, with higher values indicating better performance. The formula of calculating TSS can be expressed as follows [91]:

$$\mathrm{TSS} = \frac{4(1+R)^2}{\left(\sigma_o + \frac{1}{\sigma_o}\right)^2 (1+R_o)^2} \tag{12}$$

where R and σ_o are the correlation coefficient and ratio of STD between modeled and reference dataset, respectively, and R_o is the maximum possible correlation coefficient value, which is 1.

J. Wavelet Transform Coherence (WTC)

The WTC was used to analyze the coherent variability between runoff and climate teleconnections (ENSO and IOD) across the studied basins. The WTC has strong ability to demonstrate the mutual high energy area and phase relation in some sequences [100]. This technique has been widely employed by numerous scholars to analyze the synchronous fluctuations between atmospheric circulations and hydroclimatic variables [100], [128], [129]. The details on WTC can be found in [130].

IV. RESULTS AND ANALYSIS

A. Patterns of Water Storage and Water Balance Fluxes

Fig. 3 shows the interannual and intraannual patterns of Prec, ET, TWS, and its change (dS/dt) over the five major African basins between 2003 and 2019. For each variable, Table III lists the value of mean annual, range, and the average of wet and dry seasons.

The 17-year mean Prec calculated from the TRMM was 678.25, 1504, 705.1, 975.5, and 359.7 mm for the NRB, CRB, NIRB, ZRB, and ORB, respectively. Seasonally, the Nile [see Fig. 3(f)] and Niger [see Fig. 3(h)] basins received the highest Prec signals during JJA (June–August), and the lowest during DJF (December–February). Likewise, the Zambezi [see Fig. 3(i)] and Orange [see Fig. 3(j)] basins exhibited their maximum levels of rainfall during DJF, and the minimum during JJA. In the Congo basin [see Fig. 3(g)], the largest Prec was observed during SON (September–November), while the least during JJA.

ET is an essential component of the hydrological cycle that plays a vital role in the water budgets variations in river basins. Here, we utilized two estimates of ET extracted from MODIS and GLEAM products to determine changes in runoff across the studied basins. This was achieved by integrating the ET and Prec data into GRACE/GRACE-FO observations based on the water balance framework. From Fig. 3, the two ET time series exhibited similar distribution patterns during both the inter- and intraannual phases, with some differences in amplitude. The mean annual ET derived from MODIS and GLEAM in the period of 2003–2019 was 603.7 and 477.9 mm for the Nile, 1149 and 1210 mm for the Congo, 627.8 and 449.5 mm for the Niger, 735.4 and 601 mm for the Zambezi, and 339.7 and 167.2 mm for the Orange basin. The difference in ET performances is attributed mainly to the differences in input forcing datasets (e.g., land cover) and method structures (e.g., modeling approaches) employed for the generation of different ET products. Fig. 3 further demonstrates that both the ET sequences were in good agreement with the observed Prec changes in all basins, with the exception of the Congo basin. For example, the seasonality of the highest and lowest Prec and ET signals in the Nile basin [see Fig. 3(h)] occurred simultaneously during the JJA and DJF, respectively. While in the Congo basin, there was a distinction

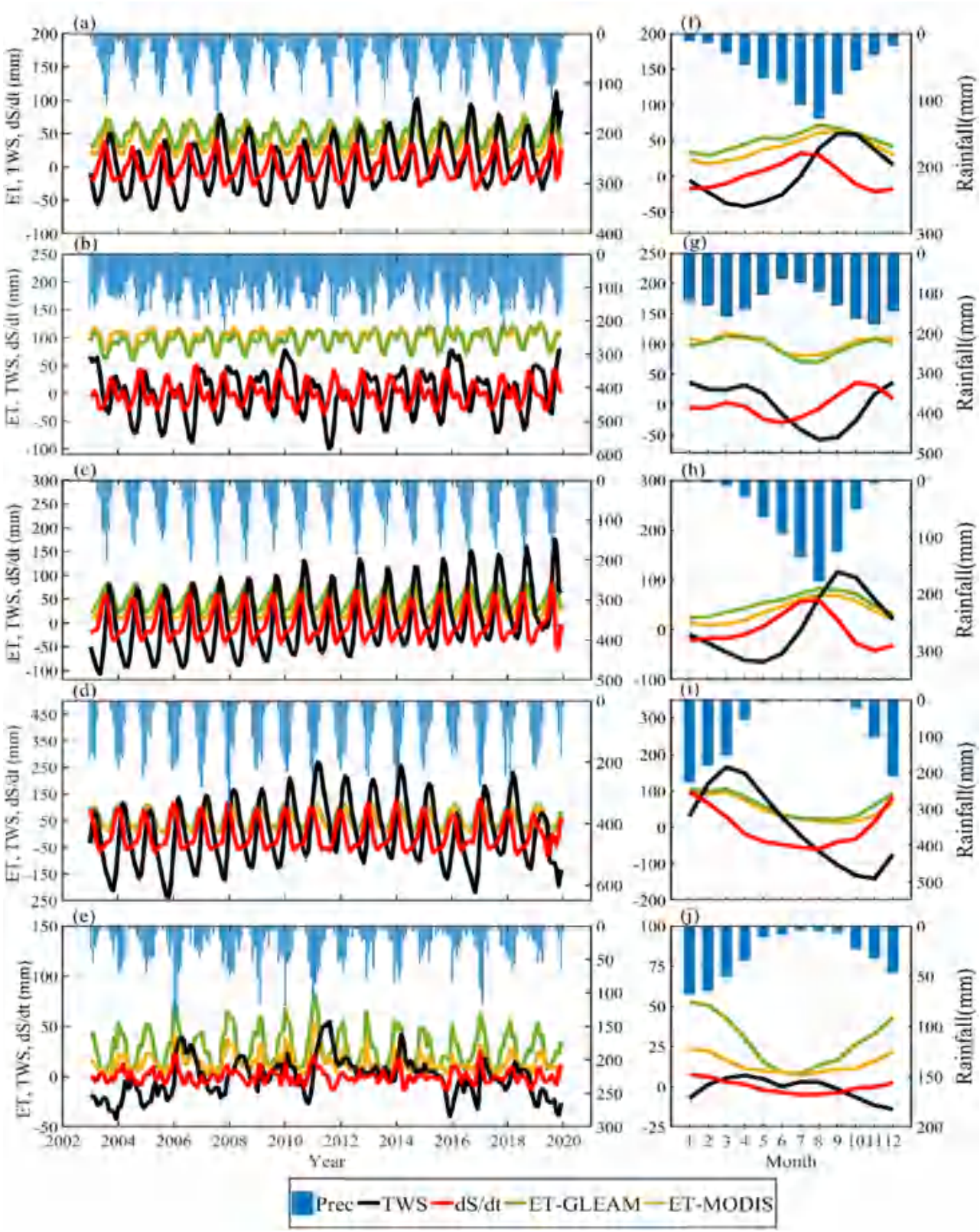

Fig. 3. (a)–(e) Interannual and (f)–(j) intraannual fluctuations time series of Prec (P), ET, TWS, and TWSC (dS/dt) in Nile (a), (f), Congo (b), (g), Niger (c), (h), Zambezi (d), and ORB (e), (j).

TABLE III
STATISTICAL REPORT OF ANNUAL AND SEASONAL VALUES OF *P*, ET, TWS, AND *dS/dT* DURING 2003–2019 FOR THE FIVE MAJOR BASINS IN AFRICA (UNITS IN MM)

Basin	Storage /fluxes	Range	Ann. mean	Wet season	Dry season
Nile	Prec	11.5–128.3	678.3	Jun.–Aug. (102.9)	Dec.–Feb. (14.7)
	TWS	–42.2 to 59.7	42.2	Sep.–Nov. (52.05)	Mar.–May. (–38.6)
	dS/dt	–21.4 to 32.2	6.0	Jun.–Aug. (26.6)	Dec.–Feb. (–18.8)
	ET-MODIS	29.9–71.7	603.7	Jun.–Aug. (61.4)	Dec.–Feb. (34.9)
	ET-GLEAM	17.8–36.5	477.9	Jun.–Aug. (61)	Dec.–Feb. (23.8)
Congo	Prec	65.6–177.7	1504	Sep.–Nov. (157.4)	Jun.–Aug. (77.9)
	TWS	–57.6 to 36.5	–4.8	Dec.–Feb. (32.7)	Sep.–Nov. (–46.2)
	dS/dt	–29.7 to 35.8	0.6	Sep.–Nov. (27.6)	Jun.–Aug. (–24.8)
	ET-MODIS	70.1–112.4	1149	Mar.–May. (109.4)	Jun.–Aug. (75.6)
	ET-GLEAM	80.4–117.5	1210	Mar.–May. (112.4)	Jun.–Aug. (82.9)
Niger	Prec	1.5–177.9	705.1	Jun.–Aug. (136.3)	Dec.–Feb. (2.4)
	TWS	–60.2 to 110	109.2	Sep.–Nov. (93.6)	Mar.–May. (–56.9)
	dS/dt	–41.7 to 58.2	5.9	Jun.–Aug. (48.7)	Dec.–Feb. (–23.5)
	ET-MODIS	24.4–82.2	627.8	Jun.–Aug. (71.4)	Dec.–Feb. (27.1)
	ET-GLEAM	9.5–69.9	449.5	Jun.–Aug. (59.2)	Dec.–Feb. (14.7)
Zambezi	Prec	1.9–227.5	975.5	Dec.–Feb. (205.8)	Jun.–Aug. (2.8)
	TWS	–140.9 to 165	38.25	Mar. –May. (133.5)	Sep.–Nov. (–125.4)
	dS/dt	–60.2 to 96.7	–1	Dec.–Feb. (82.8)	Jun.–Aug. (–47.5)
	ET-MODIS	20.6–104.1	735.4	Dec.–Feb. (98.8)	Jun.–Aug. (26.9)
	ET-GLEAM	11.5–96.9	601	Dec.–Feb. (83.7)	Jun.–Aug. (23.8)
Orange	Prec	4.5–68.3	359.7	Dec.–Feb. (60.1)	Jun.–Aug. (6.3)
	TWS	–14 to 6.9	–16.9	Mar.–May. (5.6)	Sep.–Nov. (–6.7)
	dS/dt	–5.0 to 7.3	–0.1	Dec.–Feb. (5.4)	Jun.–Aug. (–4.5)
	ET-MODIS	8.1–52.4	339.7	Dec.–Feb. (48.6)	Jun.–Aug. (10)
	ET-GLEAM	7.1–22.8	167.2	Dec.–Feb. (22.3)	Jun.–Aug. (8.3)

in the seasonality of ET and Prec (i.e., ET peaking in MAM (March–May) and Prec peaking in SON (see Table III). A prior study by Burnett et al. [131] on the ET variations in the Congo basin also found an imbalance in the peak of ET and Prec during the rainy season, which supports our findings. The authors attributed this disagreement to a number of environmental drivers that may also control ET variation, such as diffused photosynthetically active radiation fraction, net radiation, and vapor-pressure deficit.

The results derived from GRACE/GRACE-FO datasets revealed diverse patterns in water storage (TWS) across different basins and time periods (see Fig. 3). The highest and lowest variation in TWS signals was detected in the Zambezi [see Fig. 3(d)] and Orange [see Fig. 3(e)] basins, with values ranging from –140.9 to 165 mm and –14 to 6.9 mm, respectively. Furthermore, there was a time lag between the GRACE/GRACE-FO-derived TWS and Prec across the different basins. For instance, in the Zambezi basin [see Fig. 3(i)], the maximum Prec amount was seen in January, while the highest TWS value appeared in March. Overall, the change in TWS was clearly observable during the season following the change in Prec in all the basins (see Table III). When water enters the hydrosphere as Prec and it is converted to TWS during the water distribution process, there is the possibility of a theoretically delayed response between TWS and Prec [132]. The interactions between climate variables and the hydrosphere, as well as the geographical peculiarities of each basin, are the primary driving forces behind the time lag between TWS and Prec [26]. In this

study, TWS derived from GRACE/GRACE-FO showed a strong correlation with Prec, exhibiting a lag of two months in the NRB, CRB, NIRB, and ZRB and a lag of three months in the ORB.

The estimated TWSCs (dS/dt) from (2) disclosed fluctuating signals ranging from positive to negative (see Fig. 3). The Zambezi [see Fig. 3(d)] and Orange [see Fig. 3(e)] basins exhibited the highest and lowest fluctuations in dS/dt signals, with values ranging from –60.2 to 96.7 mm and –5 to 7.3 mm, respectively. Moreover, our results revealed a strong agreement between the seasonality of the maximum dS/dt and Prec signals over all the basins (see Table III). The availability of water storage in structures such as lakes, rivers, and reservoirs is generally greater during the rainy season. During and after Prec events, soil moisture and groundwater storage also increase, leading to a higher TWS, which encompasses surface water in water bodies, soil moisture, and groundwater [6]. It was observed that the dS/dt signals were predominantly negative for most of the year. Specifically, the most extreme negative dS/dt signals occurred during the DJF period in the NRB and NIRB regions and during JJA in the CRB, ZRB, and ORB regions. However, water usage for purposes such as irrigation, industrial needs, and environmental flow requirements, combined with significant evaporation and ET losses before the rainy season, contributes to the negative dS/dt [6].

Based on the displayed results in Fig. 3 and those reported in the literature [120], [133], [134], there are several discrepancies between TWS and dS/dt that can be determined. First, the sign and amplitude of TWS and dS/dt have various meanings. In this context, positive and negative TWS refer to whether the TWS during specific periods (such as a month or year) is greater than or less than its time-series mean. In contrast, positive or negative dS/dt indicates a water storage surplus or deficit during a certain period compared to a previous period. Higher TWS amplitude indicates greater regional water storage, while a higher absolute value of dS/dt ($|dS/dt|$) signifies a more rapid exchange of water storage within the regional hydrological cycle. In addition, the original TWS values derived from GRACE/GRACE-FO incorporate data from both the current month and the previous month (at times $t-1$ and t). In contrast, dS/dt is determined solely by the inputs and outputs at the current time, reflecting the changes between the first and last days of the month. Overall, dS/dt is more directly related to other water balance terms (e.g., Prec and ET) than TWS. Therefore, in this study, we convert TWS signals to dS/dt to facilitate integration with other components of the water cycle (i.e., Prec and ET) in the water balance equation.

B. Distributions of GRACE/GRACE-FO Estimated Runoff

Figs. 4–6 illustrate the spatiotemporal characteristics of the GRACE/GRACE-FO-derived runoff estimates over the major African basins during 2003–2019. For the estimation of runoff, an array of GRACE/GRACE-FO water storage change estimates, TRMM Prec measurements, and ET estimations from MODIS and GLEAM products were combined through the water budget closure framework. Due to the utilization of different ET records, two runoff estimates from GRACE/GRACE-FO were retrieved as follows: (GRACE/GRACE-FO_TRMM_MODIS)-R and (GRACE/GRACE-FO_TRMM_GLEAM)-R, which, hereafter, will be referred to as GRACE-M-R and GRACE-G-R, respectively.

The monthly average spatial distribution of the two GRACE/GRACE-FO runoff estimates over the five large African basins is shown in Fig. 4(a)–(j). A substantial variation in the spatial distribution of runoff amount is visible for all the basins. Moreover, the discrepancies between the two GRACE-GRCE-FO runoff estimates are attributed mainly to the differences in input forcing datasets (particularly the ET) for the generation of runoff. Meanwhile, the highest (175–180 mm) and lowest (around 0 mm) runoff values were found in correspondence of the southern and northern parts of the Nile basin [see Fig. 4(a) and (f)], respectively, as indicated by both GRACE/GRACE-FO runoff estimates. Within the Congo basin [see Fig. 4(b) and (g)], the extreme (130–135 mm) runoff values were detected over the central zones, while the lowest (0 mm) values were observed over the southeastern zones. For the Niger basin [see Fig. 4(c) and (h)], the southern parts received the highest (150–155 mm) amount of runoff. The runoff amount was further found to be decreasing toward the northern parts, reaching 0 mm. In the Zambezi basin [see Fig. 4(d) and (i)], the northern areas recorded the highest (110–120 mm) runoff values, while the southern areas experienced the lowest (17–20 mm) values. In case of the Orange basin [see Fig. 4(e) and (j)], the maximum (38–70 mm) runoff values were found in the eastern zones; more so, the runoff amount demonstrated to decline toward the western zones, where runoff drops to 0 mm.

Overall, the variability in runoff estimates is affected by several critical factors, such as the variations in rainfall amount, land and topography cover, vegetation type, and morphology of the soil. For example, across the Nile basin, the higher runoff amounts in the southern regions were mainly due to the presence of Lake Victoria, which represents the source of the White Nile, one of the major tributaries of the NRB. In contrast, the lower runoff rates in the northern regions were primarily due to the limited availability of Prec, as these areas are part of the Sahara Desert.

To enhance the visualization of the patterns derived from GRACE/GRACE-FO runoff estimates across the study domain, we mapped the spatial seasonal runoff patterns for the four seasons—MAM, JJA, SON, and DJF—using the GRACE-G-R estimates since it exhibits better performance in representing runoff changes in the studied basins (see Section III-C). This is illustrated in Fig. 5.

Obviously, the seasonal cycle has significant effects on runoff patterns across all basins. In the Nile basin [see Fig. 5(a)–(d)], the runoff amount increases from MAM to JJA, with the highest contribution observed during JJA over the eastern parts, and decreases from SON to DJF with the lowest contribution during DJF. This finding is in line with the results of previous study of Abd-Elbaky and Jin [48] over the NRB. Within the Congo basin [see Fig. 5(e)–(h)], the runoff values increase from JJA to SON and from DJF to MAM, respectively. However, the maximum seasonal runoff was observed during SON over the central zones,

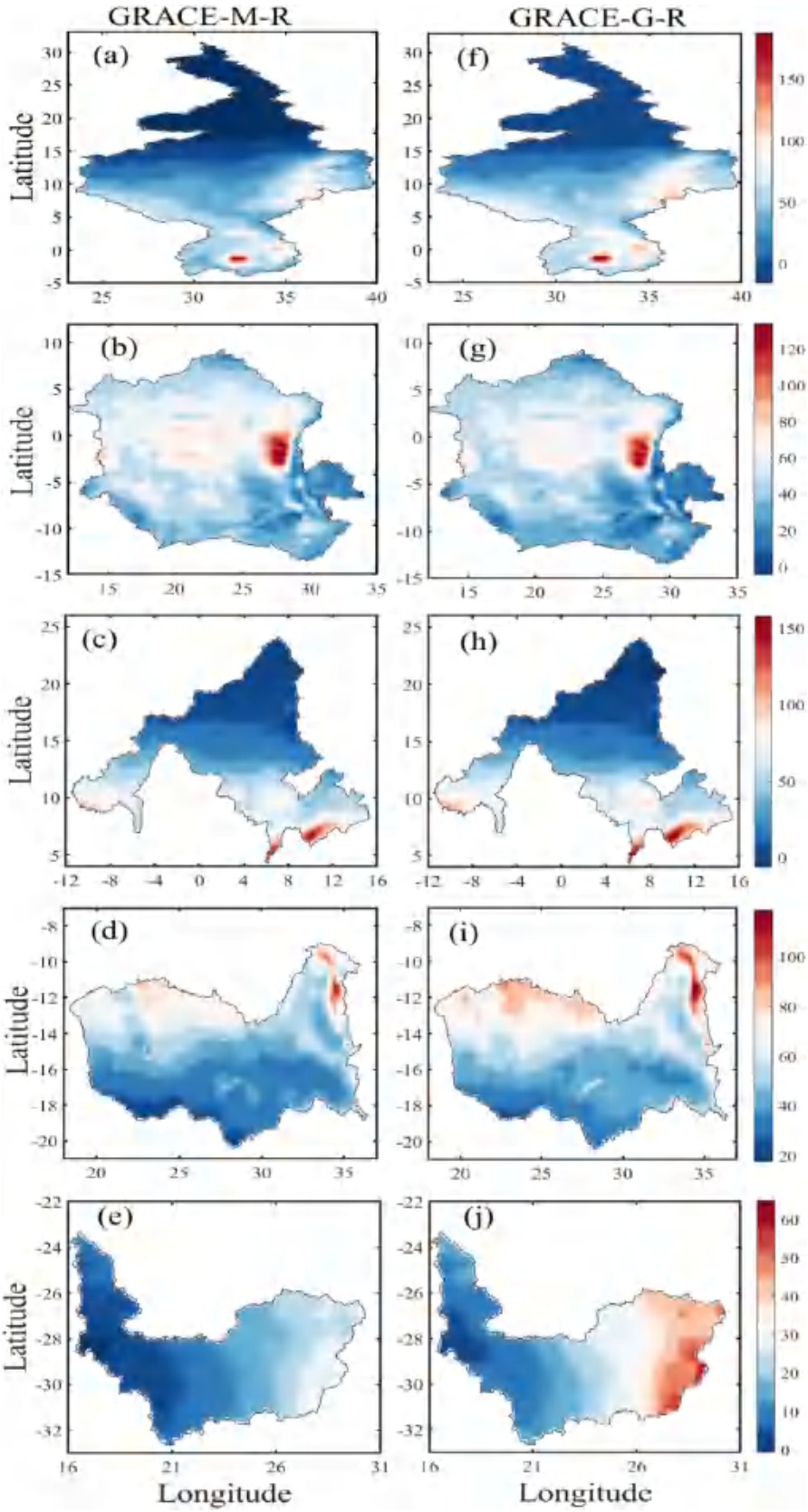

Fig. 4. Spatial distribution of the estimated runoff from GRACE/GRACE-FO during 2003–2019 over (a), (f) Nile, (b), (g) Congo, (c), (h) Niger, (d), (i) Zambezi, and (e), (j) Orange basins.

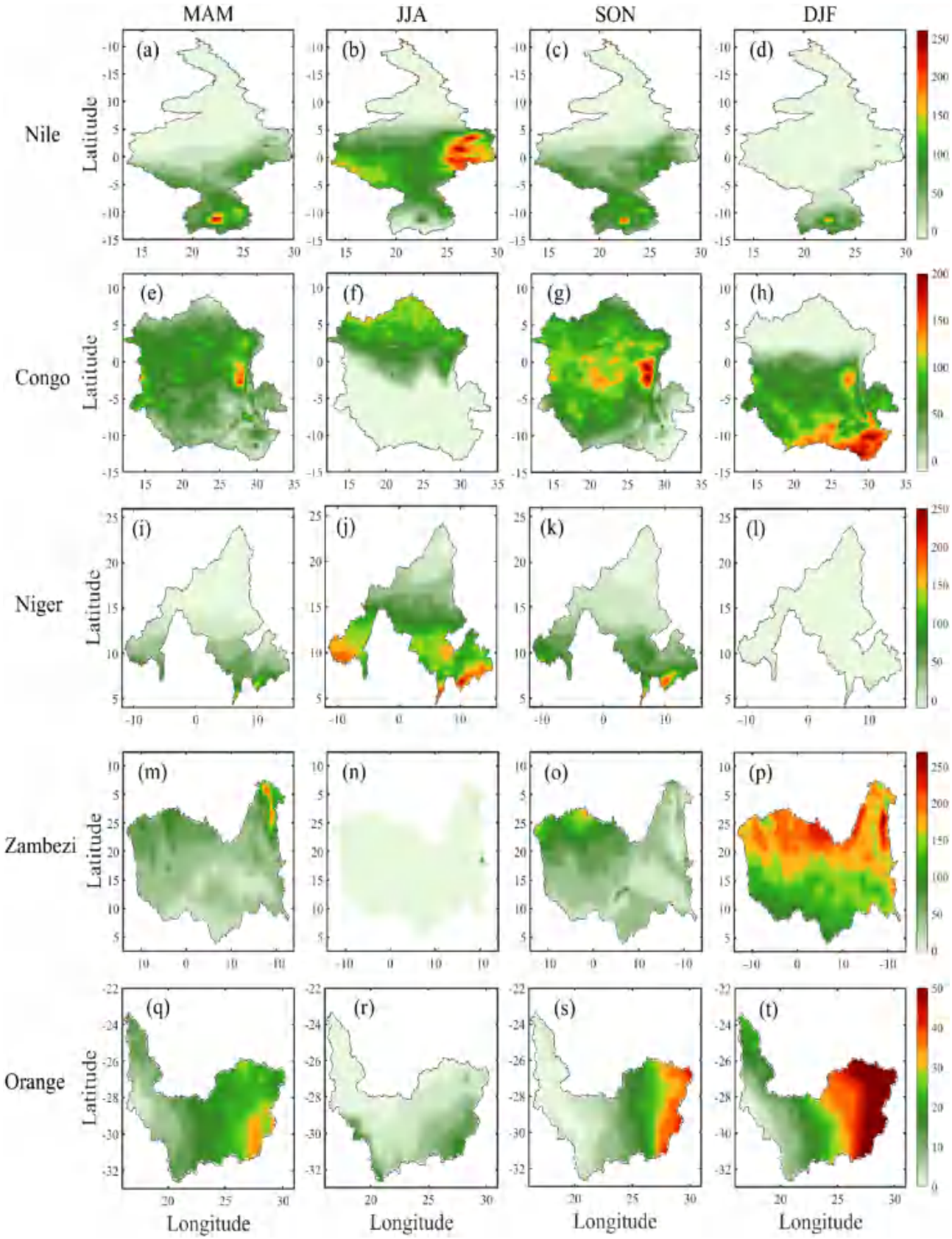

Fig. 5. (a)–(t) Spatial seasonal distribution of the estimated runoff from GRACE/GRACE-FO during 2003–2019 in major African basins.

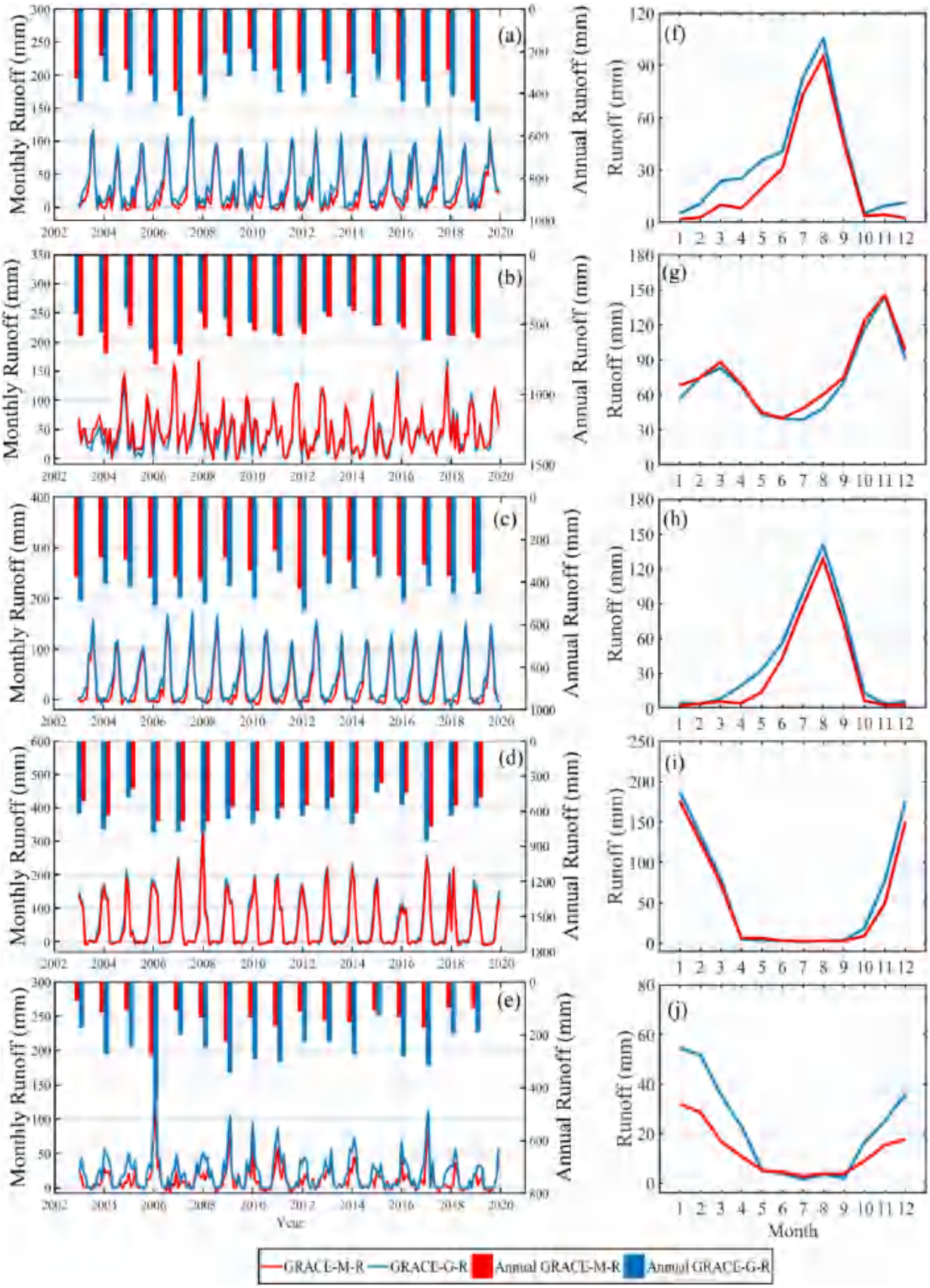

Fig. 6. Temporal distribution of the estimated runoff from GRACE/GRACE-FO during 2003–2019 over (a), (f) Nile, (b), (g) Congo, (c), (h) Niger, (d), (i) Zambezi, and (e), (j) Orange basins.

whereas the minimum was recorded during JJA. The Niger basin [see Fig. 5(i)–(l)], on the other hand, demonstrated similar seasonal features to the Nile basin, where the runoff amount increases from MAM to JJA and decreases from DJF to SON. The largest runoff amount was observed over the southern areas during JJA, while the smallest amount was registered during DJF. Efon et al. [62] investigated the spatial seasonal distribution of runoff over West Africa and indicated that the peak of runoff occurred in JJA, which is consistent with our findings over the Niger basin. In the Zambezi basin [see Fig. 4(m)–(p)], the runoff amount rises from SON to DJF, with the highest contribution observed during DJF over the upper zones, and declines from MAM to JJA with the lowest contribution during JJA. The Orange basin [see Fig. 5(q)–(t)], however, revealed comparable seasonal characteristics to the Zambezi basin, in which runoff amount increases from SON to DJF and decreases from MAM to JJA. The maximum seasonal runoff was observed during DJF over the eastern zones, while the minimum was detected during JJA.

Fig. 6 displays the annual, interannual, and intraannual temporal distribution of the two GRACE/GRACE-FO runoff estimates over the large African basins during 2003–2019. A clear fluctuation in the temporal patterns of runoff is apparent for all the basins. The highest runoff amount was seen in 2019, 2006, 2012, 2017, and 2006 and the lowest in 2010, 2014, 2011, 2015, and 2015 for the NRB, CRB, NIRB, ZRB, and ORB, respectively [see Fig. 6(a)–(e)]. The results from the intraannual variability indicated that runoff in the Nile and Niger [see Fig. 6(f) and (g)] basins increases from January to the peak at August and basically decreases from August to December. Alghafli et al. [49] analyzed the intraannual runoff variability over the Nile basin and indicated similar results to our findings. Efon et al. [62] characterized runoff variation over West Africa between 1981 and 2021 using ERA5 and reported that the large values of runoff are observed in July and August, which is in line with our results for the Niger basin. In the Congo basin [see Fig. 6(h)], runoff rises from January to March and then decreases until June. It increases again until November, before dropping once more in December. In the Zambezi and Orange basins [see Fig. 6(i) and (j)], runoff decreases from its peak in January to its lowest point in July, before rising again until December. In general, the differences in runoff patterns can be attributed to the varying climatological and hydrological backgrounds of the basins.

For instance, in the Niger basin, the lower runoff observed in January is due to the dry season in West Africa [135]. Conversely, the high runoff levels in August result from the significant rainfall during that period (see Fig. 3).

C. Comparison of Runoff Estimation From GRACE/GRACE-FO

In this work, the reliability of runoff estimates from GRACE/GRACE-FO is evaluated by comparing them with estimations from numerous runoff product, including the GLDAS (using NOAH, VIC, and CLM models), the ERA5, and the SCS-CN. Details of runoff estimates from SCS-CN are described above in Section III. Fig. 7 shows the interannual and intraannual distribution of seven runoff time series across the five large African basins between 2003 and 2019.

Clearly, all the time series exhibit a similar pattern of runoff over both the inter- and intraannual phases, with remarkable differences in amplitude. For example, in the Nile and Niger basins [see Fig. 7(f) and (h)], the seven runoff sequences showed an increase from January to August, reached the maximum in August, and declined gradually from August to December. This result suggests an overall good agreement between the two GRACE/GRACE-FO-derived runoff estimates and the five other runoff products. Our results further revealed that both the GRACE/GRACE-FO runoff estimates, alongside the SCS-CN, notably overestimate the amplitude of runoff during the rainy seasons in all the basins. Mohanasundaram et al. [6] calculated runoff estimates over United States basins using GRACE data and observed overestimated runoff values during the wet season, which is parallel to our finding. Chen et al. [41] and Alghafli et al. [49] also pointed out that during the rainy season, river runoff estimates obtained from in-situ gauges in the Amazon and upper Blue Nile basins tend to underestimate those derived from GRACE. The authors attributed this underestimation to uncertainties associated with the in-situ gauges during the rainy seasons. The SCS-CN, on the other side, is basically a rainfall-runoff model, and its algorithm relies on transforming rainfall to runoff. Hence, as the Prec was the primary factor considered in modeling runoff, the outcome runoff exhibits higher magnitude during the wet seasons than in other products. It is worth noting that the discrepancy in magnitude among GRACE/GRACE-FO runoff estimates and global runoff products (i.e., NOAH, CLM, VIC, and ERA5) may also reflect the fact that these global products are incapable to adequately capture runoff magnitude during the wet seasons.

In addition to the visual comparisons described earlier, numerical comparison analyses were run between the two GRACE/GRACE-FO runoff estimates and the other five runoff products (i.e., NOAH, VIC, CLM, ERA5, and SCS-CN). Two performance metrics were employed for the comparison, namely, Pearson's correlation coefficient (r) and TSS. The closer the value of TSS and r to 1, the better in agreement between GRACE/GRACE-FO-derived runoff estimates and other five runoff products.

The Pearson's r values between the two GRACE/GRACE-FO runoff estimates and the five other runoff products for the NRB, CRB, NIRB, ZRB, and ORB were greater than 0.80, 0.60, 0.88, 0.84, and 0.80, respectively (see Fig. 8). Likewise, the TSS values obtained for the NRB, CRB, NIRB, ZRB, and ORB were higher than 0.58, 0.58, 0.67, 0.44, and 0.29, respectively, when compared the five runoff products to the two GRACE/GRACE-FO runoff estimations (see Fig. 9). Overall, the performance of the datasets generated using GRACE/GRACE-FO satellites was satisfactory, as the calculated statistical indicators were within the acceptable range. The difference in scores produced by different products is mainly attributed to the disparities in models' structure and input datasets utilized for each product's calculation.

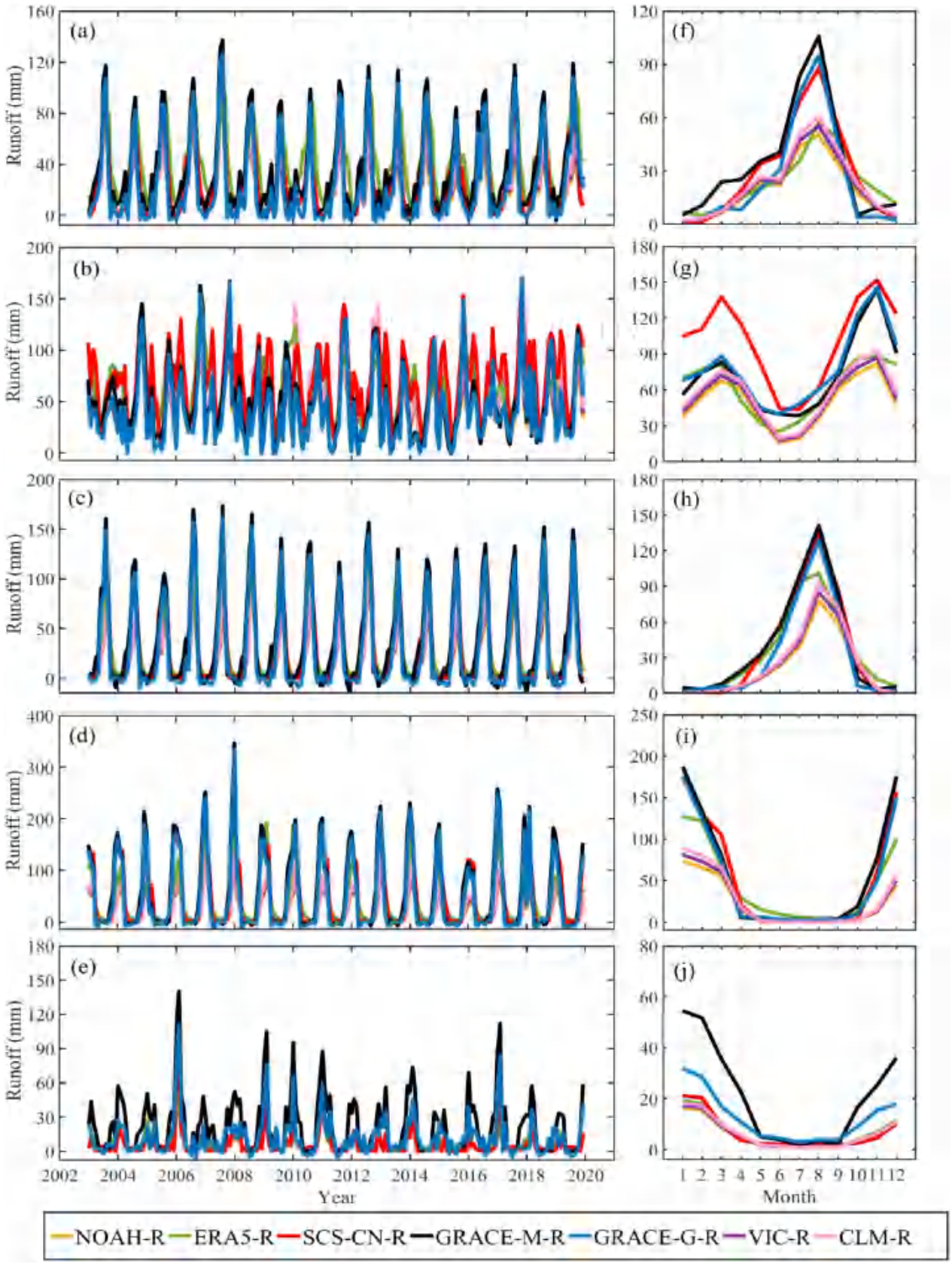

Fig. 7. Inter- and intraannual runoff time series from three solutions of GLDAS (CLM, NOAH, and VIC) and those estimated by ERA5, SCS-CN, and GRACE/GRACE-FO (GRACE-M-R and GRACE-G-R) during 2003–2019 over Nile (a), (f), Congo (b), (g), Niger (c), (h), Zambezi (d), (i), and Orange (e), (j) river basins.

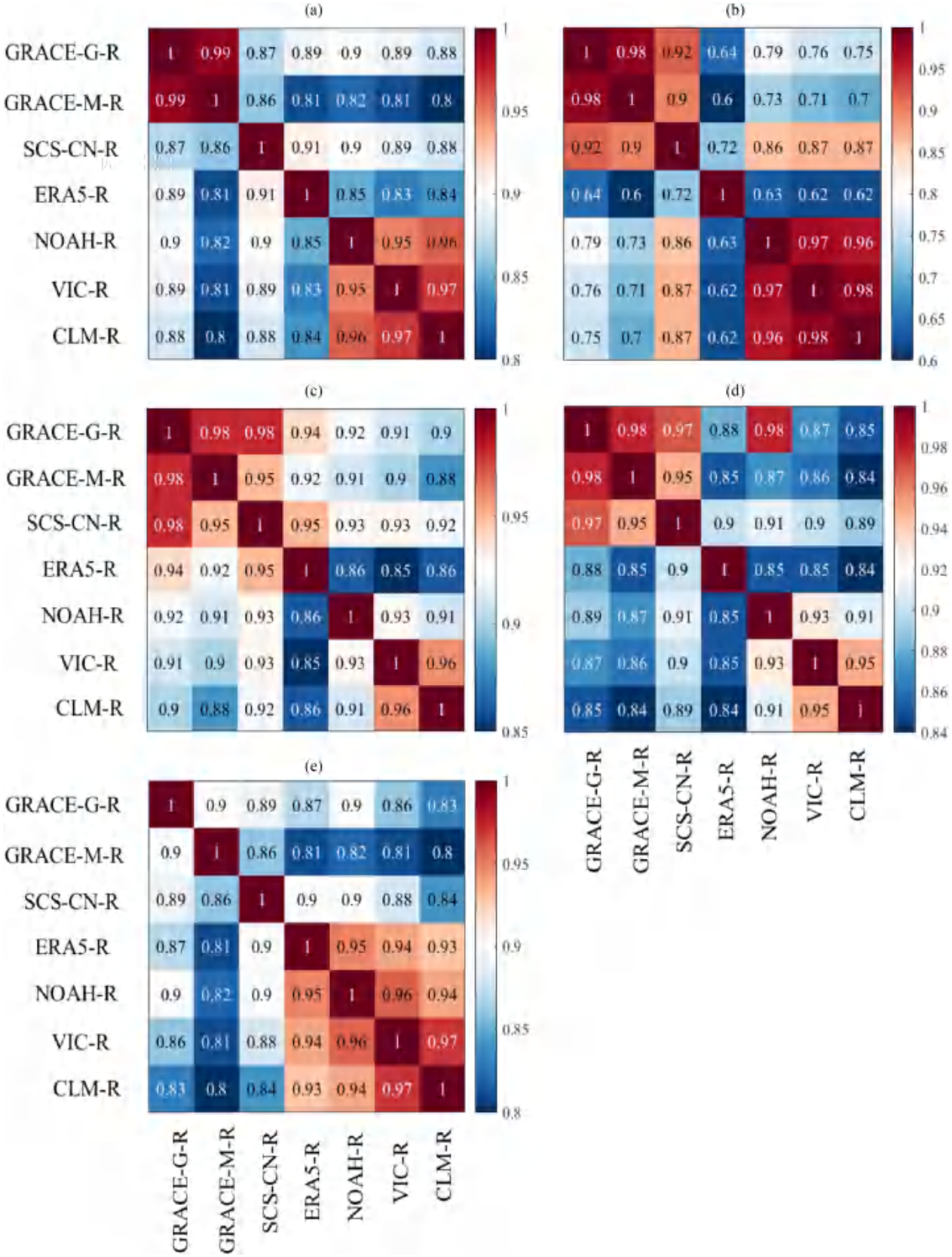

Fig. 8. Pearson correlation coefficient matrix between the estimated runoff by GRACE/GRACE-FO (GRACE-M-R, GRACE-G-R) and those estimated from GLDAS (NOAH, VIC, and CLM), ERA5, and CSC-CN. (a) Nile. (b) Congo. (c) Niger. (d) Zambezi. (e) Orange.

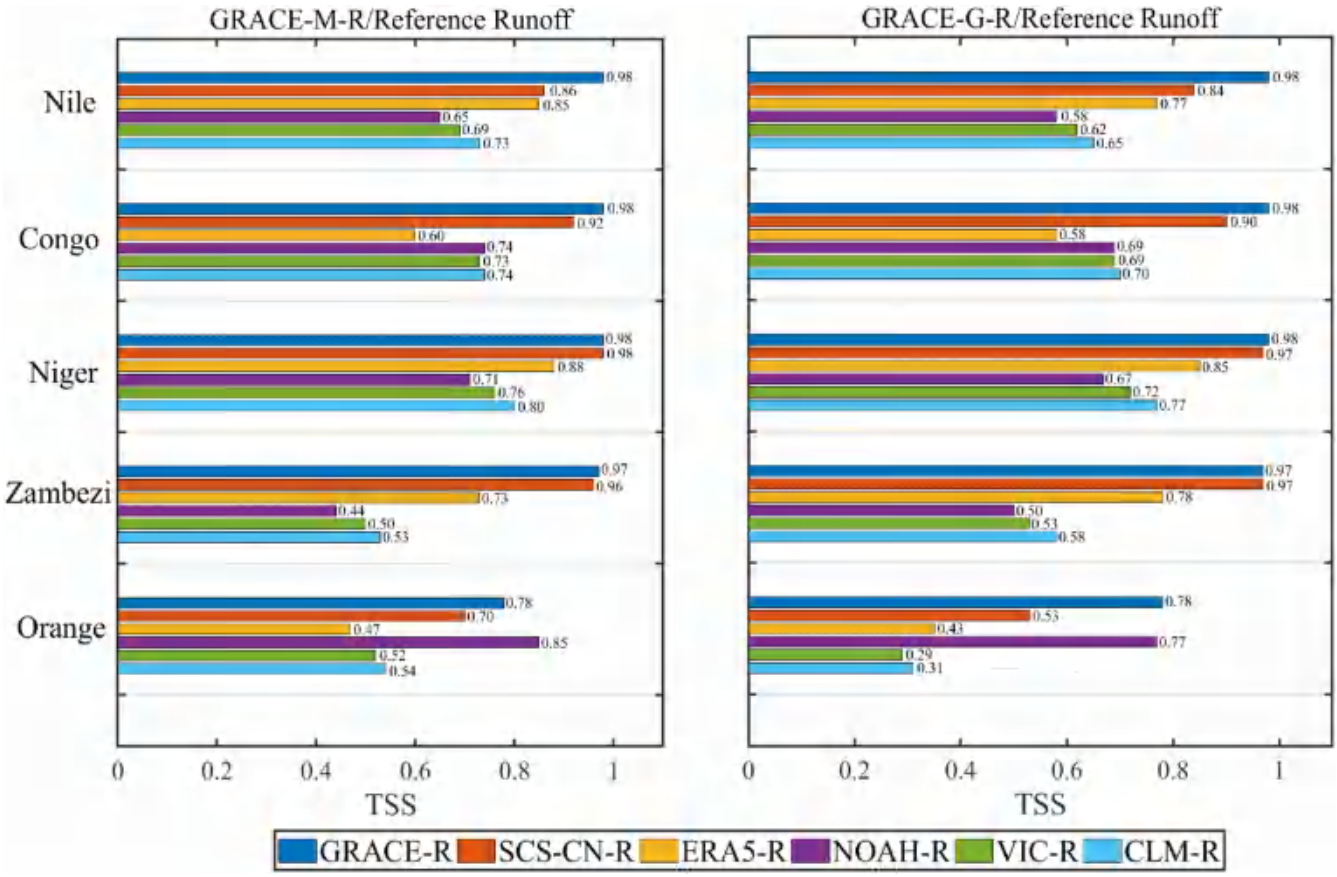

Fig. 9. TSS between the estimated runoff by GRACE/GRACE-FO (GRACE-M-R and GRACE-G-R) and those estimated from GLDAS (NOAH, VIC, and CLM), ERA5, and CSC-CN.

Moreover, among the five products, the SCS-CN exhibited the highest Taylor scores and Pearson coefficient values versus the two GRACE/GRACE-FO runoff estimates in most basins. The robust relationship between the runoff estimates from GRACE/GRACE-FO and SCS-CN may be attributed to the inclusion of similar Prec data (i.e., TRMM) in their calculations. On the other hand, this study employed three different types of models to compare with the GRACE/GRACE-FO runoff estimates. These models include empirical/ local rainfall-runoff model (SCS-CN), land surface runoff model (GLDAS solutions), and reanalysis runoff model (ERA5). The runoff estimates from GRACE/GRACE-FO showed the strongest correlation with those from the SCS-CN (see Figs. 8 and 9), suggesting that the GRACE/GRACE-FO estimates may represent rainfall-runoff in the studied basins. To clarify this further, we examined the runoff-to-precipitation (runoff/precipitation) ratio for all products using the annual mean Prec and runoff data (see Fig. 10). The results indicated that, in most basins, both the GRACE/GRACE-FO runoff estimates and SCS-CN exhibit significantly higher runoff/precipitation values compared to other runoff products. This elevated runoff/precipitation ratio indicates a greater contribution of Prec to the total runoff estimated by these models. Therefore, based on the findings reported in Fig. 10, it may be concluded that the runoff amounts estimated by GRACE/GRACE-FO are induced mainly by Prec. In other words, Prec is the primary driver of GRACE/GRACE-FO runoff estimates over the considered basins. This finding further supports the assertion that the GRACE/GRACE-FO runoff estimates act as rainfall-runoff in the vast African basins.

Furthermore, it has been proven that local hydrological models, such as SCS-CN, exhibit lower uncertainty and greater accuracy in simulating runoff at basin scale compared to global models [11]. Hence, the strong harmony between GRACE/GRACE-FO runoff estimates and SCS-CN may also indicate that the GRACE/GRACE-FO method is more reliable and effective in modeling regional scale-runoff, compared to global hydrological models and global LSMs. Mohanasundaram et al. [6] compared different runoff estimates from GRACE and GLDAS-LSM to in-situ observations in United States basins and concluded that the GRACE runoff estimates are more robust than the GLDAS-LSM at the regional scale, which could support our study findings.

The results in Figs. 8 and 9 further depicted that, in most basins, the GRACE-G-R estimates yielded slightly better agreement with the five runoff products, compared to GRACE-M-R. This result suggests that the accuracy of GRACE/GRACE-FO runoff estimates is better captured through combining GLEAM (ET), TRMM (Prec), and GRACE/GRACE-FO (dS/dt) than combining MODIS (ET), TRMM (Prec), and GRACE/GRACE-FO (dS/dt). In other words, using GLEAM ET data enhances the

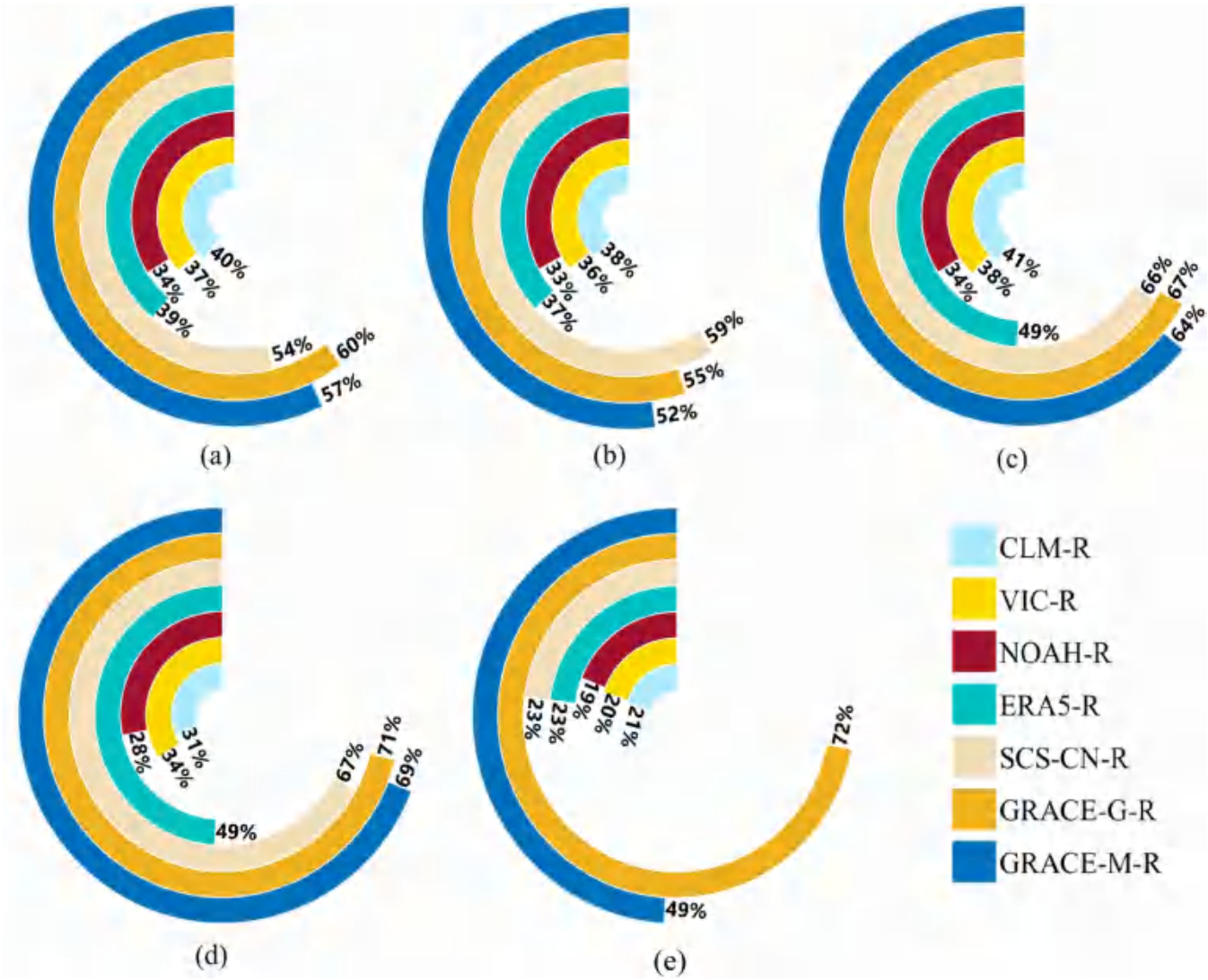

Fig. 10. Runoff-to-precipitation ratios across major basins in Africa based on different runoff simulations. (a) Nile. (b) Congo. (c) Niger. (d) Zambezi. (e) Orange.

agreement between estimated basins runoff and reference runoff dataset. Alghafli et al. [49] calculated runoff in the portion of the NRB using a water balance approach, incorporating seven Prec products, three ET products (MOD16, Penman-Monteith-Leuning (PML), and GLEAM), and two TWS products. They found that GLEAM outperformed both MOD16 and PML, producing the best results, which supports our findings. In addition, MOD16 and GLEAM were evaluated over 837 global catchments, yielding similar results to ours, confirming that GLEAM outperformed MOD16 [136]. Consequently, we propose using GRACE-G-R estimates to represent runoff variations in the river basins considered for the rest of this study.

D. Runoff Changes and Their Possible Linkages With Climate Factors

1) Detection of Mutation Point: As previously discussed, the monthly runoff time series demonstrates considerable seasonal variability (see Fig. 6), which may influence the mutation point test. To mitigate the effects of seasonality and accurately identify the change point, we initially removed the seasonal trend from the original runoff time series utilizing the STL method. Following the deseasonalization of the monthly runoff data, we identified the mutation point for each basin employing the Pettitt nonparametric test, with the results presented in Table IV. To enhance our understanding of runoff responses to climate change, we divided the entire study period (RA, from 2003 to 2019) into two segments: R1 (premutation period) and R2 (postmutation period, inclusive of the mutation year) for each basin. This temporal division is similarly applied in the analysis of other variables, such as Prec and Temp, to further investigate the effects of climatic factors on runoff changes.

2) Runoff Trends: Seasonal runoff for each basin and their trend slopes are shown in Fig. 11. Looking into Fig. 11, seasonal runoff exhibits distinct patterns across different basins and time periods. From 2003 to 2019 (RA), seasonal runoff in the Nile basin [see Fig. 11(a) and (f)] showed increasing trend slopes, ranging from 0.12 (MAM, $p < 0.05$) to 0.46 mm/a (SON,

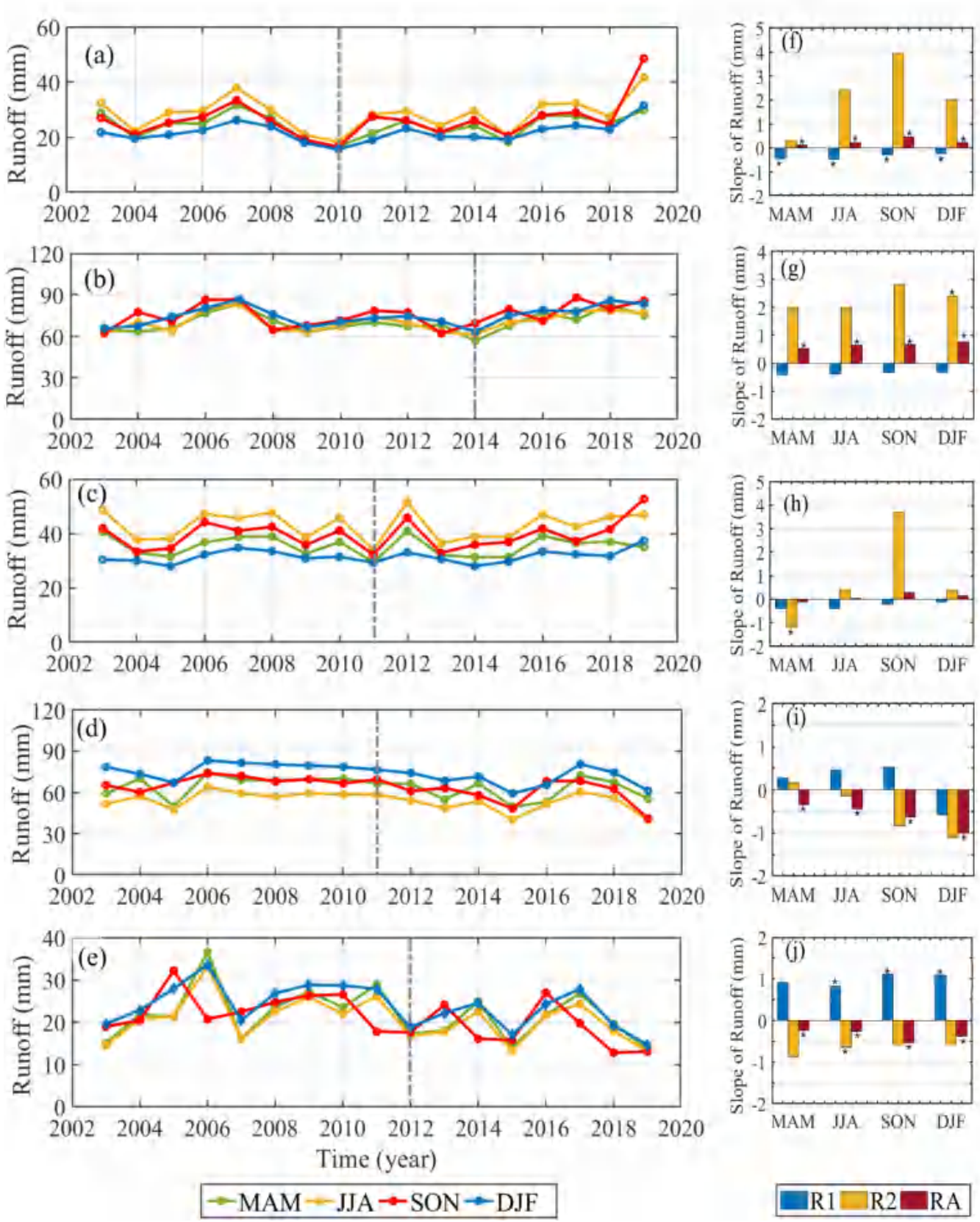

Fig. 11. Seasonal runoff (MAM, JJA, SON, and DJF) during 2003–2019 in the (a) Nile, (b) Congo, (c) Niger, (d) Zambezi, and (e) Niger, and their trend slope (rate of change) in the (f) Nile, (g) Congo, (h) Niger, (i) Zambezi, and (j) Orange during the premutation (R1), postmutation (R2), and whole periods (RA). $*$ indicates significant liner trends at 5% confidence level.

TABLE IV
MUTATION POINTS OF MONTHLY RUNOFF IN EACH BASIN

Basin	Mutation point
Nile	Jan. 2010
Congo	Jul. 2014
Niger	Mar. 2011
Zambezi	Jun. 2011
Orange	Apr. 2012

Note that $p < 0.05$ in all basins.

$p < 0.05$). Higher increasing trends (0.31–3.95 mm/a) were found during R2, while significant decreasing trends (–0.47 to –0.23 mm/a) were observed during R1. Within the Congo basin [see Fig. 11(b) and (g)], seasonal runoff during RA showed rising trend slopes, ranging between 0.52 (MAM, $p < 0.05$) and 0.76 mm/a (DJF, $p < 0.05$). From R1 to R2, runoff slopes changed from higher negative (–0.41 to –0.32 mm/a) to higher positive (2 to 2.38 mm/a). In RA, seasonal runoff in the Niger basin [see Fig. 11(c) and (h)] showed declining trend slope during MAM (–0.1 mm/a), and rising trend slopes during JJA (0.04 mm/a), SON (0.27 mm/a), and DJF (0.16 mm/a). More so, across JJA, SON, and DJF, runoff slopes decreased first in R1 (–0.04 to –0.21 mm/a) and then increased in R2 (1.74 to 4.9 mm/a), but it decreased in both R1 and R2 during MAM. For the Zambezi basin [see Fig. 11(d) and (i)], seasonal runoff in RA illustrated decreasing trend slopes, ranging from –1 (DJF, $p < 0.05$) to –0.34 mm/a (MAM, $p < 0.05$). Furthermore, all seasons except DJF revealed increasing slopes (0.27–0.52 mm/a) during R1, whereas all seasons except MAM revealed decreasing slopes (–1.11 to 0.15 mm/a) during R2. In case of the Orange basin [see Fig. 11(e) and (j)], seasonal runoff during RA illustrated decreasing trend slopes, ranging from –0.54 (SON, $p < 0.05$) to –0.24 mm/a (MAM, $p < 0.05$). Besides, positive trend slopes (0.82–1.11 mm/a) were found during R1, while negative trend slopes (–0.88 to –0.59 mm/a) were observed during R2.

Overall, the highest change in RA was found during SON season in the Nile ($p < 0.05$), Niger, and Orange ($p < 0.05$) basins, and during DJF season in the Congo ($p < 0.05$) and Zambezi ($p < 0.05$) basins. In addition, the change in RA throughout these sensitive seasons mainly came from the change in R2.

3) Possible Linkages Between Runoff Changes and Climate Factors: Here, we investigated the linkages between climate variables: Temp and Prec with runoff. We quantified the trends in climate forcing and analyzed its relationship with runoff variabilities in each basin. In addition, we explored the correlations between runoff, LST, and Prec for the period 2003–2019 using Pearson's correlation coefficient (r) to better understand their controlling roles.

Fig. 12 displays the seasonal trend slopes in Prec and Temp over the five major African basins during the premutation period (Prec1, Temp1), postmutation period (Prec2, Temp2), and the entire period (Prec A, Temp A). From 2003 to 2019, seasonal Prec in the Nile and Congo basins [see Fig. 12(a) and (b)] showed upward trends during all seasons, with values ranging from 0.17 (MAM, $p < 0.05$) to 0.3 mm/a (JJA, $p < 0.05$) and 0.5 (MAM, $p < 0.05$) to 0.7 mm/a (SON, $p < 0.05$) for the Nile and Congo, respectively. This finding is consistent with the runoff patterns presented in Fig. 11(a) and (b). In addition, these patterns of positive Prec slopes were also observed by Alahacoon et al. [137], who pointed to an increase in rainfall rates for the Nile and Congo basins from 1983 to 2020 during the four seasons. Similarly, Temp exhibited downward trends across the four seasons, with reads varying between –0.05 (DJF, $p<0.05$) to –0.03 °C/a (JJA, $p < 0.05$) and –0.02 (SON, $p < 0.05$) to –0.01 °C/a (MAM, $p < 0.05$) for the Nile [see Fig. 12(f)] and Congo [see Fig. 12(g)] basins, respectively. However, the Temp in the both basins depicted positive slopes during Temp1 and negative slopes during Temp2, while Prec displayed negative slopes during Prec1 and positive slopes during Prec2. This finding implies that the key driver influencing an increase in runoff in the Nile and Congo basins is climate change, characterized by an increase in Prec and decrease in Temp.

In the Niger basin [see Fig. 12(c) and (h)], seasonal Prec over 2003–2019 demonstrated rising trends through JJA (0.15), SON (0.16), and DJF (0.18) mm/a. In contrast, MAM observed a declining trend with a read of –0.05 mm/a. However, these changes were not statistically significant ($p > 0.05$) in all seasons. Temp, on the other side, showed records of 0.04, –0.001, –0.013, and –0.002 °C/a for MAM, JJA, SON, and DJF, respectively. These slopes also did not pass the significant level ($p > 0.05$). During the premutation period, all seasons showed negative trends in Prec and positive trends in Temp. Contrarily, the postmutation period exhibited diverse trends across the different seasons.

In the case of Zambezi and Orange basins [see Fig. 12(d) and (e)], seasonal Prec showed downward trends during 2003–2019 period, with values ranging from –0.9 (DJF, $p < 0.05$) to –0.55 mm/a (MAM, $p < 0.05$) and –0.7 (SON, $p < 0.05$) to –0.45 mm/a (MAM, $p < 0.05$) for the Zambezi and Orange basins, respectively. This finding corroborates with the runoff patterns demonstrated in Fig. 11(i) and (j), denoting that Prec is substantially controlling the runoff fluctuations in these basins. Moreover, this result is substantiated by the findings of Nhemachena et al. [138] who indicated a significant decline in Prec over Southern Africa during the past decade. Simultaneously, Temp depicted an upward trend throughout the given seasons, with reads varying between 0.05 (SON, $p < 0.05$) to 0.08 °C/a (JJA, $p < 0.05$) and 0.1 (MAM and DJF, $p < 0.05$) to 0.2 °C/a (SON, $p < 0.05$) for the Zambezi and Orange basins, respectively. NourEldeen et al. [103] analyzed the changes in LST over the entire Africa during 2003–2017 era. They demonstrated that LST increases over most parts of Southern Africa throughout the given seasons, which supports the findings of our study. However, in both basins, Temp illustrated negative slopes during Temp1 and positive slopes during Temp2, whereas Prec showed positive slopes during Prec1 and negative slopes during Prec2. This finding indicates that changes in climate have substantial contribution to runoff reductions in the Zambezi and Orange basins, evidenced by the decrease in Prec and

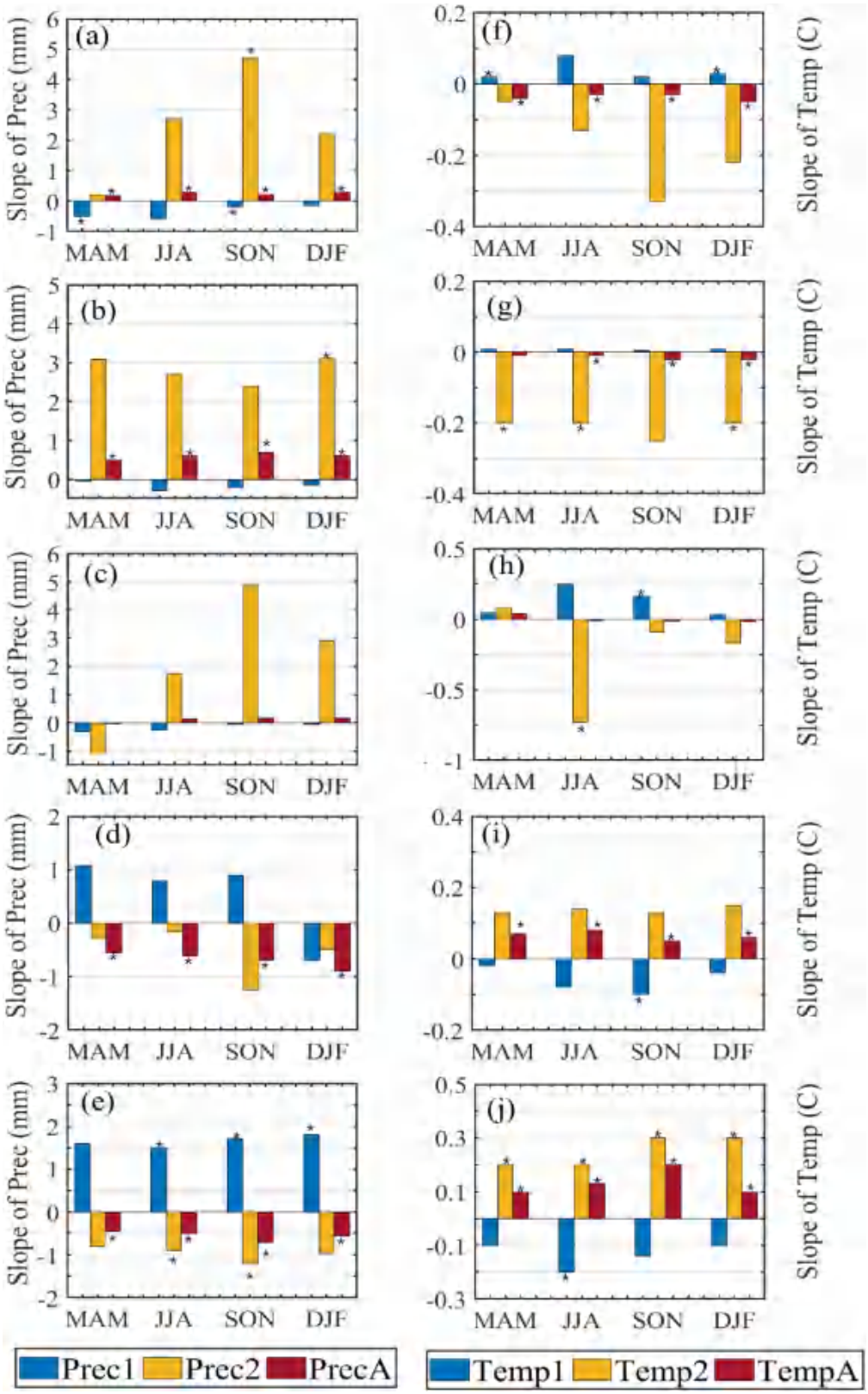

Fig. 12. Seasonal trend slopes (MAM, JJA, SON, and DJF) in Prec and Temp over the (a), (f) Nile, (b), (g) Congo, (c), (h) Niger, (d), (i) Zambezi, and (e), (j) Orange basin during the premutation (Prec1, Temp1), postmutation (Prec2, Temp2), and whole periods (PrecA, TempA). $*$ indicates significant liner trends at 5% confidence level.

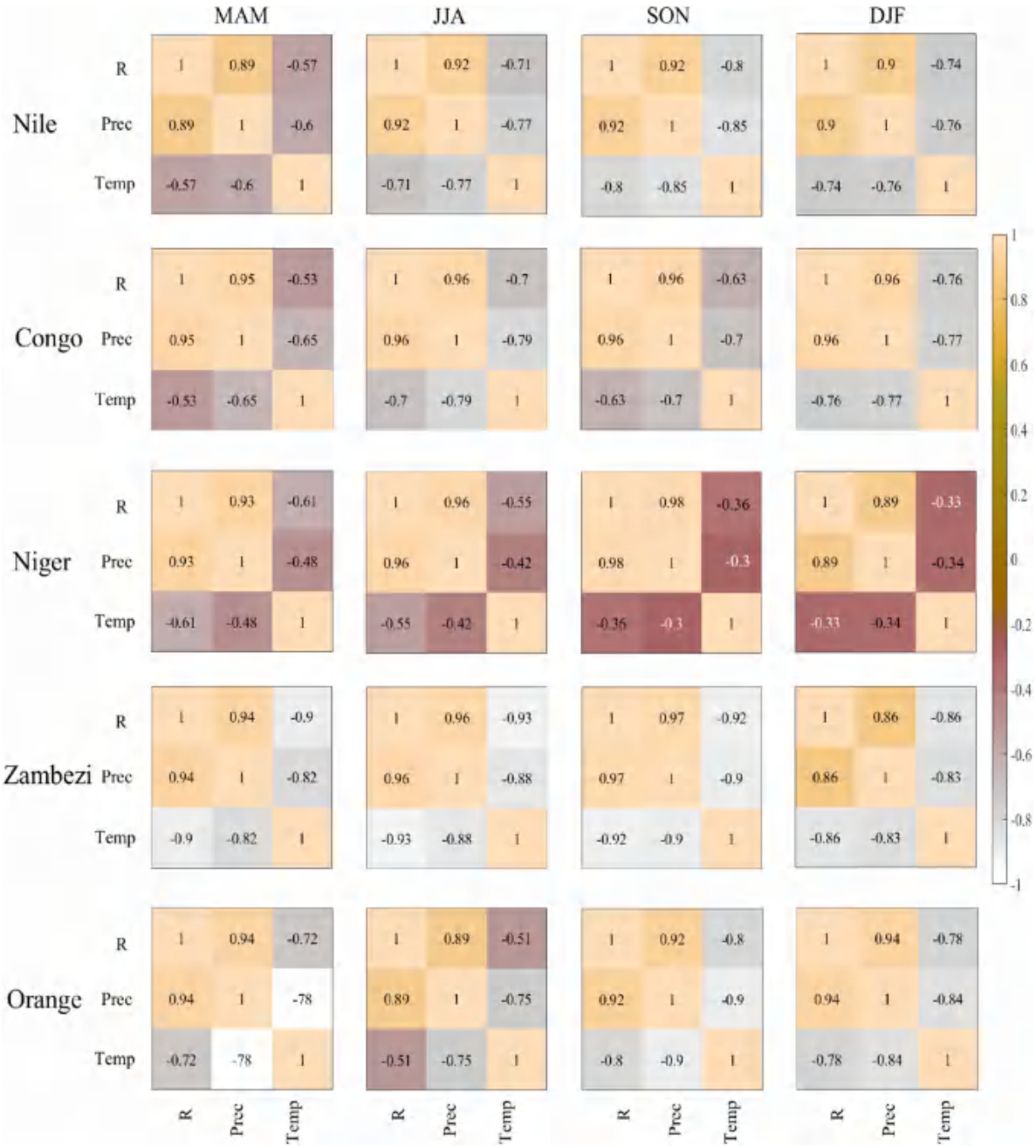

Fig. 13. Pearson's correlation coefficients between runoff (*R*), Prec, and Temp during the four seasons.

the increase in Temp. Moreover, future estimates for Southern Africa demonstrate reduced rainfall and increased Temps, which drive significant regional implications such as water stress, food and energy insecurity, and extreme droughts [138], [139], [140].

To enhance the understanding of how climate variables influence changes in runoff, this study calculated Pearson's correlation coefficients (*r*) among runoff, Temp, and Prec across the four seasons, as shown in Fig. 13.

On the whole, there was significant correlation (at the 95% level) between the Prec and Temp with the runoff across the four seasons in all the basins. The Pearson's *r* values between the Prec and runoff during the four seasons were within the range of 0.89–0.92, 0.95–0.96, 0.89–0.98, 0.86–0.97, and 0.89–0.94 for the NRB, CRB, NIRB, ZRB, and ORB, respectively. This result denotes that the Prec has a positive impact on runoff changes across the understudied basins. Furthermore, it demonstrates that the positive impacts of Prec on runoff are persistent over the whole year (i.e., during the four seasons; see Fig. 13).The maximum *r* between Prec and runoff was recorded in JJA and SON over the Nile, JJA and SON and DJF over the Congo, SON over the Niger and Zambezi, and DJF and MAM over the Orange. This finding indicates that the response of runoff to Prec variations was stronger during these seasons than in others. The minimum *r* between Prec and runoff was observed during MAM over the Nile and Congo, DJF over the Niger and Zambezi, and JJA over the Orange.

TABLE V
MONTHS IN WHICH THE MAXIMUM (MMAX) AND MINIMUM (MMIN) OF RUNOFF OCCURRED DURING R1, R2, AND RA

	Period	Nile	Congo	Niger	Zambezi	Orange
MMax	R1	August	November	August	January	December
	R2	August	November	August	January	December
	RA	August	November	August	January	December
MMin	R1	January	July	January	July	July
	R2	January	July	January	July	July
	RA	January	July	January	July	July

Likewise, the Pearson's *r* values between Temp and runoff during the four seasons were within the range of –0.57 to –0.80, –0.55 to –0.79, –0.33 to –0.61, –0.80 to –0.93, and –0.51 to –0.80 for the NRB, CRB, NIRB, ZRB, and ORB, respectively. This finding implies that the Temp has a negative impact on runoff changes across the studied basins. It further indicates that the negative effects of Temp on runoff are persistent over the entire year. However, the largest *r* between Temp and runoff was observed in SON over the Nile and Orange basins, DJF over the Congo, MAM over the Niger, and JJA over the Zambezi basin. This finding indicates that the response of runoff to Temp changes was greater during these seasons than in others. On the contrary, the lowest *r* between the Temp and runoff was found in MAM over the Nile and Congo basins, DJF over the Niger and Zambezi basins, and JJA over the Orange basin.

In summary, the evidence indicates that climate changes significantly contribute to runoff variability in Africa's major basins, as demonstrated by the variations in Prec and Temp, along with the strong Pearson's *r* values between runoff and these climate factors. The current study identified rising Temp trends in the Zambezi and Orange basins, suggesting that these areas may become more vulnerable to extreme droughts and Temp events moving forward. Human activities significantly affect the continent's water resources, particularly in the ORB [141]. Therefore, further investigation into the effect of human activities on runoff changes is necessary.

E. Runoff Regime Alterations

In this section, we applied a framework that incorporates indicators of both interannual and intraannual runoff regimes to describe changes in the runoff system. These indicators are categorized into three groups: magnitude, variability, and duration (see Fig. 2). The analyses of the indicators influencing interannual and intraannual runoff regimes between the pre- and postmutation periods are presented as follows.

1) Runoff Magnitude: Fig. 14 illustrates the intraannual average runoff, along with Prec and Temp, for each basin during the premutation, postmutation, and overall periods. Notably, different basins display distinct runoff transition patterns from R1 to R2. In addition, the shape of the runoff hydrograph, defined by the months of highest and lowest values and their sequence (see Table V), remained relatively consistent across R1, R2, and RA for all basins. In the Nile basin [see Fig. 14(a)], runoff increased in all months, with an average monthly runoff difference (△AMR) of 5.8 mm [see Fig. 15(d)]. However, the increase from December to February was slightly less pronounced than in other months. The Congo basin [see Fig. 14(b)] also experienced an increase in runoff across all months, with a △AMR of 7.3 mm. In the Niger basin [see Fig. 14(c)], runoff increased in all months, yielding a △AMR of 3.3 mm. More so, January to May showed a slightly lower increase compared to other months. In contrast, the southern river basins, represented by the Zambezi [see Fig. 14(d)] and Orange [see Fig. 14(e)] basins, demonstrated a decrease in runoff from R1 to R2, with △AMR values of –7.4 and –4.1 mm, respectively.

The low (LMR25), median (MMR50), and high (HMR75) runoff during R1, R2, and RA were determined using the runoff's probability density function and cumulative density function (CDF) (see Fig. 15). Fig. 15(a)–(c) illustrates the absolute differences in LMR25, MMR50, and HMR75 between R1 and R2, highlighting changes in various sections of their CDF curves. In the Nile basin, small absolute differences were observed: LMR25 (4.2 mm), MMR50 (4.04 mm), and HMR75 (4.11 mm) (see Fig. 14), indicating a general increase in runoff with greater magnitudes in R2. Similar trends were noted in the Congo and Niger basins, where an overall increase in runoff was detected (i.e., the CDF curve shifts right in R2; see Fig. 15). The absolute change in MMR50 (8.85 mm) was greater than in LMR25 (7.43 mm) and HMR75 (5.81 mm) across the Congo basin. In contrast, the Niger basin exhibited a larger absolute difference in HMR75 (4.35 mm) compared to MMR50 (3.38 mm) and LMR25 (2.17 mm). The Zambezi and Orange basins displayed consistent patterns, showing a general decrease in runoff (i.e., the CDF curves shift left in R2; see Fig. 15). However, the absolute differences were greater in the Zambezi basin, with LMR25 (–6.31 mm), MMR50 (–7.04 mm), and HMR75 (–8.03 mm), compared to the Orange basin, which showed differences of –4.02, –4.05, and –4.5 mm for LMR25, MMR50, and HMR75, respectively (see Fig. 16).

In conclusion, the results from Figs. 14–16 show that the magnitude of runoff in the Nile, Congo, and Niger basins was greater during the postmutation period compared to the premutation period, indicating an overall increase in runoff in these areas. In contrast, the magnitude of runoff in the Zambezi and Orange basins was lower in the postmutation period than in the

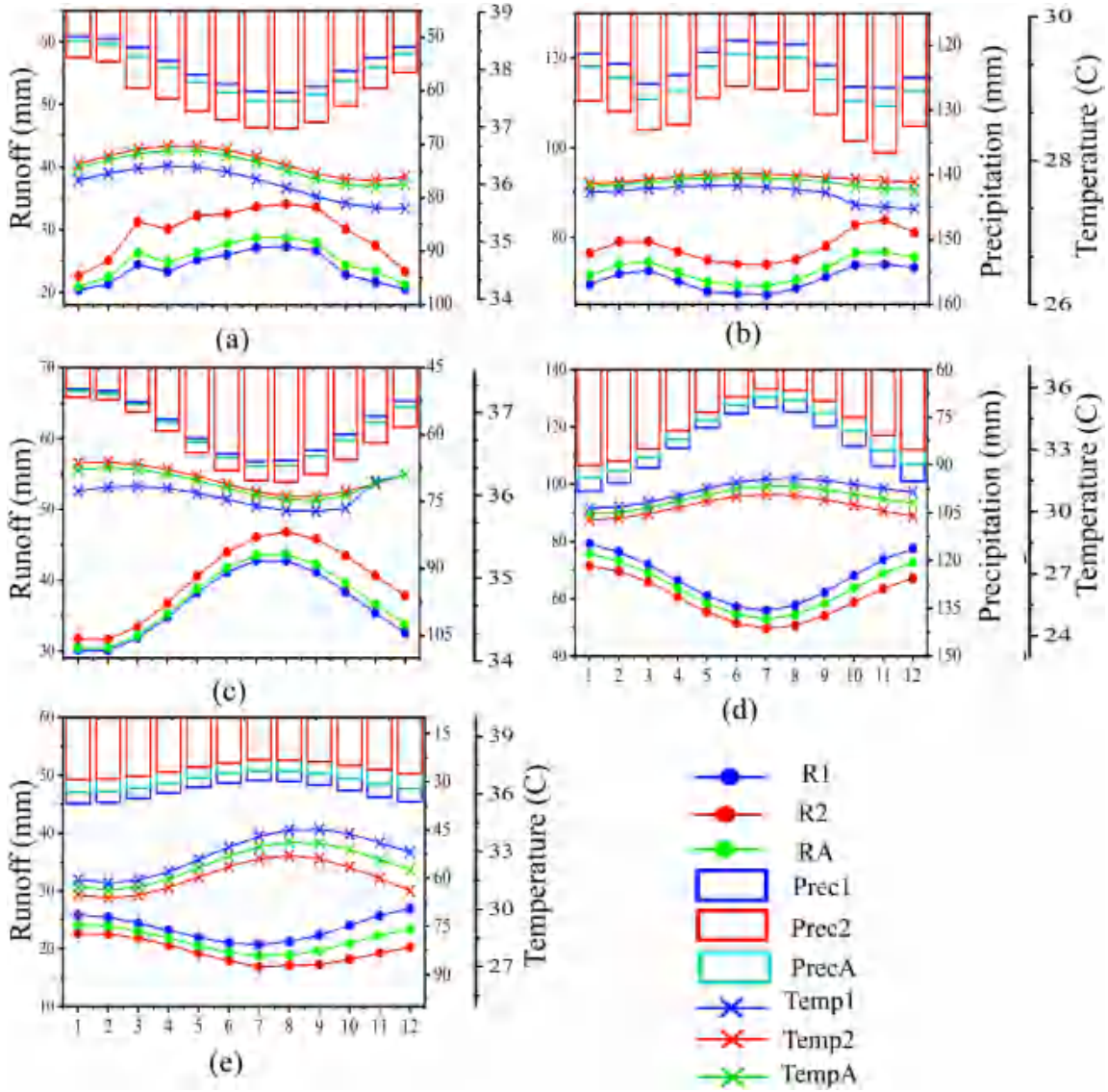

Fig. 14. Intraannual variation of runoff (*R*), Prec, and Temp during premutation period (blue color), postmutation period (red color), and the whole period (green color) in the five major basins in Africa. (a) Nile. (b) Congo. (c) Niger. (d) Orange. (e) Zambezi.

premutation period, suggesting an overall decrease in runoff in both regions.

2) Runoff Variability: To investigate intraannual runoff variability, we measured the STD and range (highest minus lowest) of multiyear mean monthly runoff during R1, R2, and RA [see Fig. 17(a) and (c)]. We further determined the relative changes in STD and range between R1 and R2, as shown in Fig. 17(b) and (d). Positive relative changes in STD and range were observed in the Nile (60% and 65%), Congo (34% and 46%), and Niger (16% and 19%) basins, suggesting an overall increase in intraannual runoff variability in these regions. As the runoff magnitude in these basins increased each month (see Fig. 14), their intraannual variability also increased from R1 to R2 [see Fig. 17(a) and (b)]. This indicates that higher runoff magnitudes are associated with greater runoff variability in these basins. Negative relative changes in STD and range, on the other side, were observed for the Zambezi (–8% and –5%) and Orange (–2% and –7%) basins, denoting an overall decline in intraannual runoff variability in both basins. Moreover, while the magnitude in the Zambezi and Orange basins decreased from R1 to R2 (see Fig. 14), their intraannual variability also declined [see Fig. 17(a) and (b)], which implies that both basins are witnessing magnitude reductions accompanied by a decrease in runoff variability.

3) Runoff Duration: For evaluating the changes in runoff duration, we first determined the median monthly runoff in RA (MMR50) for each basin utilizing the runoff CDF (see Fig. 15); next, the times (i.e., frequency) preceding MMR50 in R1 (DMR1) and R2 (DMR2) were computed [see Fig. 17(e)]. The absolute change between DMR1 and DMR2 was also obtained as depicted in Fig. 17(f). Positive absolute changes in DMR were observed in the Nile (0.27), Congo (0.35), and Niger (0.20) basins, indicating that these basins experienced an amplitude in the duration of runoff. Moreover, as the runoff magnitude and

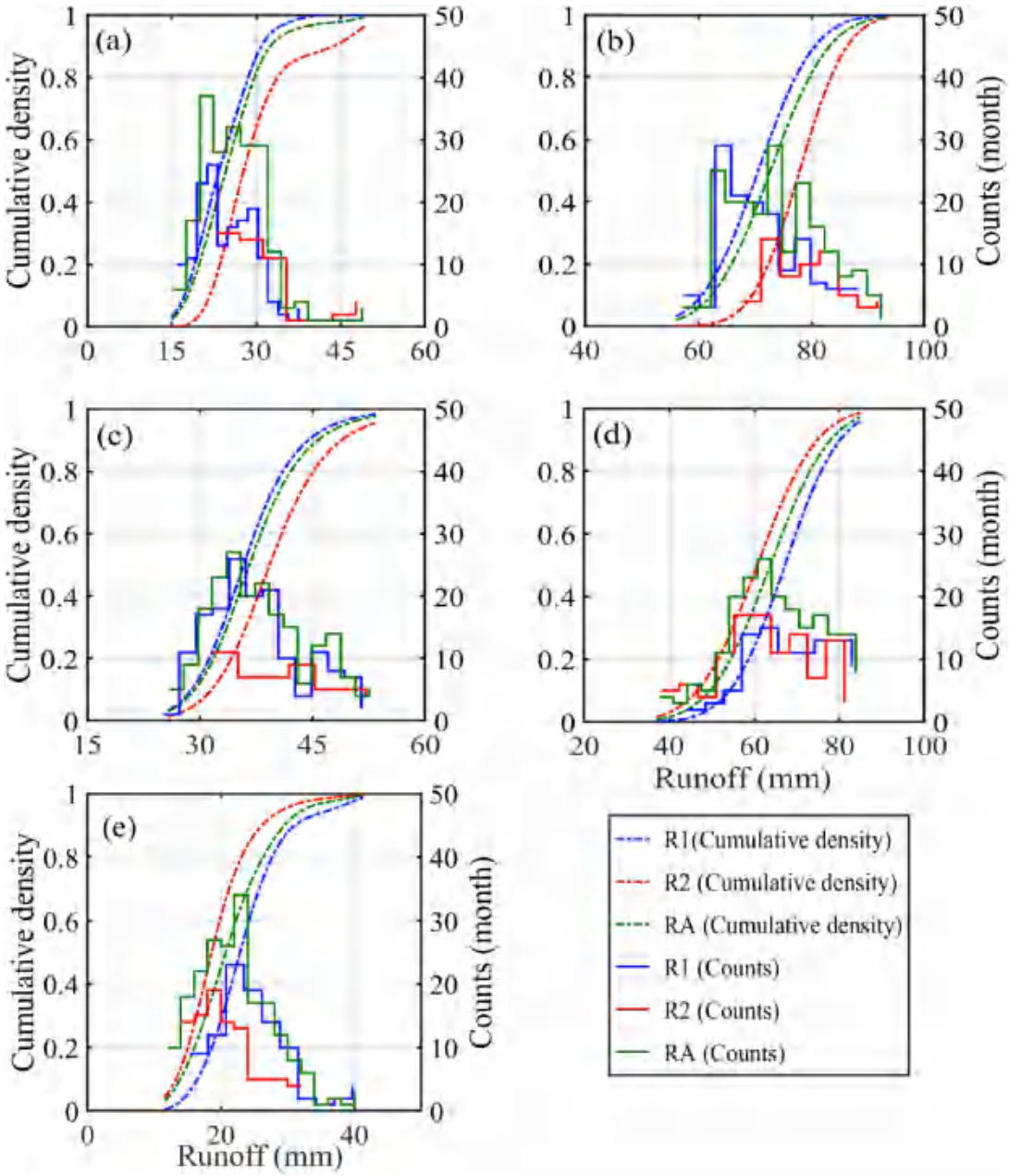

Fig. 15. Cumulative density (left *Y*-axis) and probability (frequency) distribution (right *Y*-axis) of monthly runoff during R1 (blue color), R2 (red color), and RA (green color) in the (a) Nile, (b) Congo, (c) Niger, (d) Zambezi, and (e) Orange basin.

variability increased from R1 to R2 in these basins (see Figs. 14–17), the duration also increased, suggesting that the regions witnessing a higher positive magnitude change in runoff accompanied by higher variability and increased duration. Likewise, negative absolute changes in DMR were observed in the Zambezi (–0.23) and Orange (–0.35) basins, implying that both basins witnessed reductions in the duration of runoff. However, not only the runoff magnitude and variability decreased in R2 for both basins (see Figs. 14–17), but their duration also reduced, which denotes that both basins are experiencing magnitude reductions accompanied by a lower runoff variability and a reduction in duration.

F. Influences of Climate Teleconnections on Runoff Fluctuations

Climate teleconnections reflect the natural variability of the Pacific, Indian, and Atlantic Oceans, the Mediterranean Sea, and the Arctic [142]. Early studies sought to link variations in runoff to these climate teleconnections [129], [130], [131], [132]. In this study, we focused on the ENSO and the IOD to examine their influences on runoff fluctuations in Africa's major basins during the period from 2003 to 2019. Given the relatively short duration of the study, we prioritized short-term indices such as the ENSO and IOD.

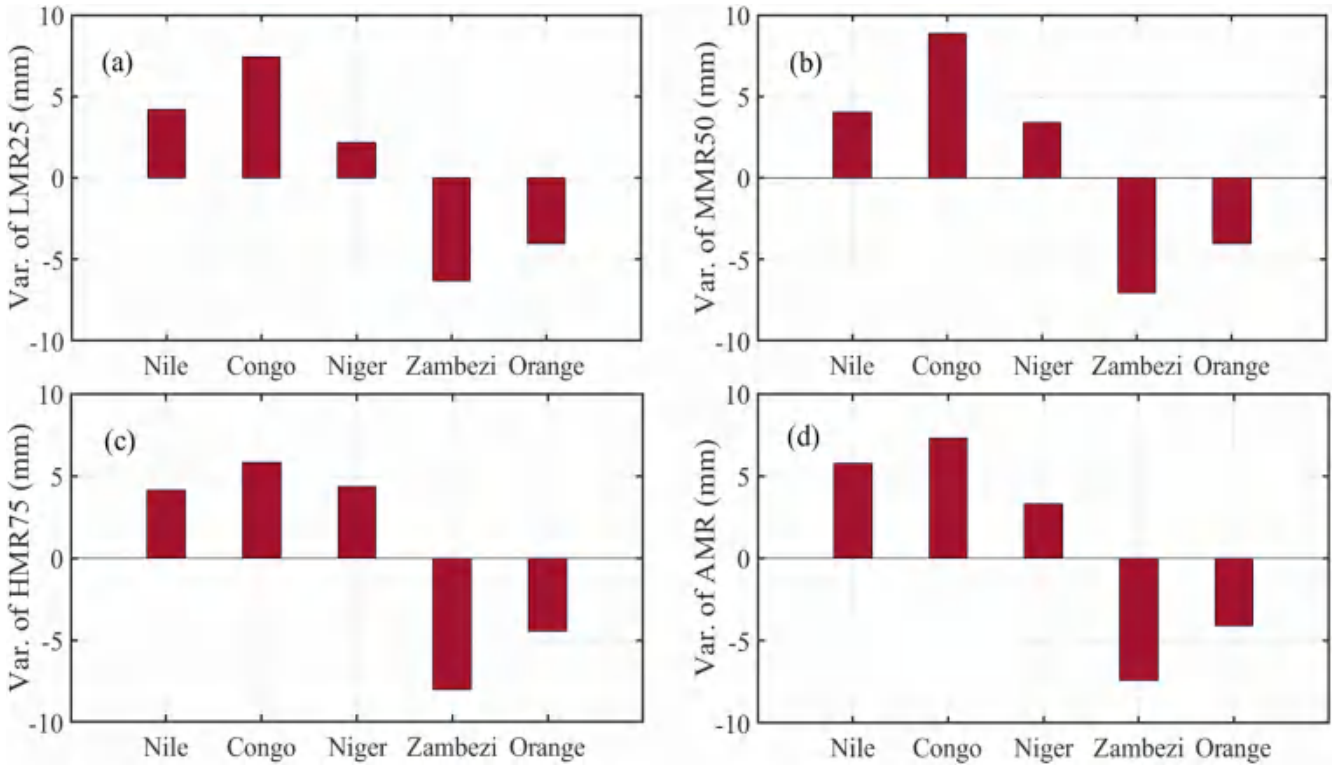

Fig. 16. Absolute difference in (a) low ($LMR25_2 - LMR25_1$), (b) median ($MMR50_2 - MMR50_1$), (c) high ($HMR75_2 - HMR75_1$), and (d) average ($AMR_2 - AMR_1$) monthly runoff between R1 and R2 in the five major basins in Africa.

The Pearson's correlation coefficients (r) between the monthly runoff and oceanic factors in African's major basins are shown in Fig. 18. As a whole, ENSO and IOD had significant impacts on the monthly scale runoff changes across all the given basins. The r between runoff and ENSO was –0.2, –0.33, –0.18, –0.38, and –0.4 for the NRB, CRB, NIRB, ZRB, and ORB, respectively. This result indicates that ENSO had negative impacts on runoff across all the basins. In contrast, the r between IOD and runoff was 0.18, 0.37, 0.28, 0.22, and –0.37 for the NRB, CRB, NIRB, ZRB, and ORB, respectively. This result implies that IOD had a positive influence on the runoff in the NRB, CRB, NRB, and ZRB, while having a negative influence on the ORB.

To better understand the roles of teleconnection factors on runoff variabilities over the study domain, we evaluated the correlations between runoff changes and teleconnection factors in each season, as illustrated in Fig. 19. In MAM, ENSO depicted a negative effect on runoff changes across all the basins, whereas IOD exhibited a positive effect across the Nile, Congo, and Niger basins. In JJA, ENSO illustrated a negative influence on runoff changes over all the basins except the Niger basin, whereas IOD displayed a positive influence over the Congo basin and a negative influence over the Orange basin. In SON, ENSO exhibited a negative impact on runoff changes in all the basins except the Nile basin. IOD, on the other hand, demonstrated a positive impact in the Congo, Niger, and Zambezi basins, while depicting a negative impact in the Orange basin. In DJF, ENSO had a negative effect on runoff changes across all the basins except the Nile basin. IOD depicted a positive effect in the Congo and Niger basins, while exhibiting a negative effect on the Orange basin.

Overall, the response of runoff to the oscillations of climate teleconnections varied from season to season, and basin to basin. The highest impact of ENSO on runoff changes occurred in JJA across the Nile, SON across the Congo and Orange, and DJF across the Zambezi and Niger basins. Besides, the largest influence of IOD on runoff changes was observed in JJA through the Nile and Niger, and SON through the Congo, Zambezi, and Orange basins.

In an attempt to enhance the robustness of this study, we further calculated the wavelet correlation coefficients between oceanic factors: ENSO and IOD with runoff changes, to explore the dynamic relation between runoff change and oceanic factors (see Fig. 20). The blue areas surrounded by the thick black lines in Fig. 20 are statistically significant at the 5% level. The direction of the arrow from left to right denotes that two signals are in-phase relationship, while the direction from right to left denotes that two signals are antiphase relationship.

In the Nile basin [see Fig. 20(a) and (b)], ENSO and runoff demonstrated significant but sporadic antiphase relationships between 2003 and 2015, at a time band ranging from 2–96 months. On the other hand, IOD and runoff illustrated a significant in-phase relationship from 2005 to 2006 at a time band of 2–4 months, and from 2011 to 2015 at a time band of 16–32 months. In addition, at a time band of 4–8 months, IOD and runoff exhibited in-phase and antiphase relationship from 2010 to 2011 and 2012 to 2014, respectively.

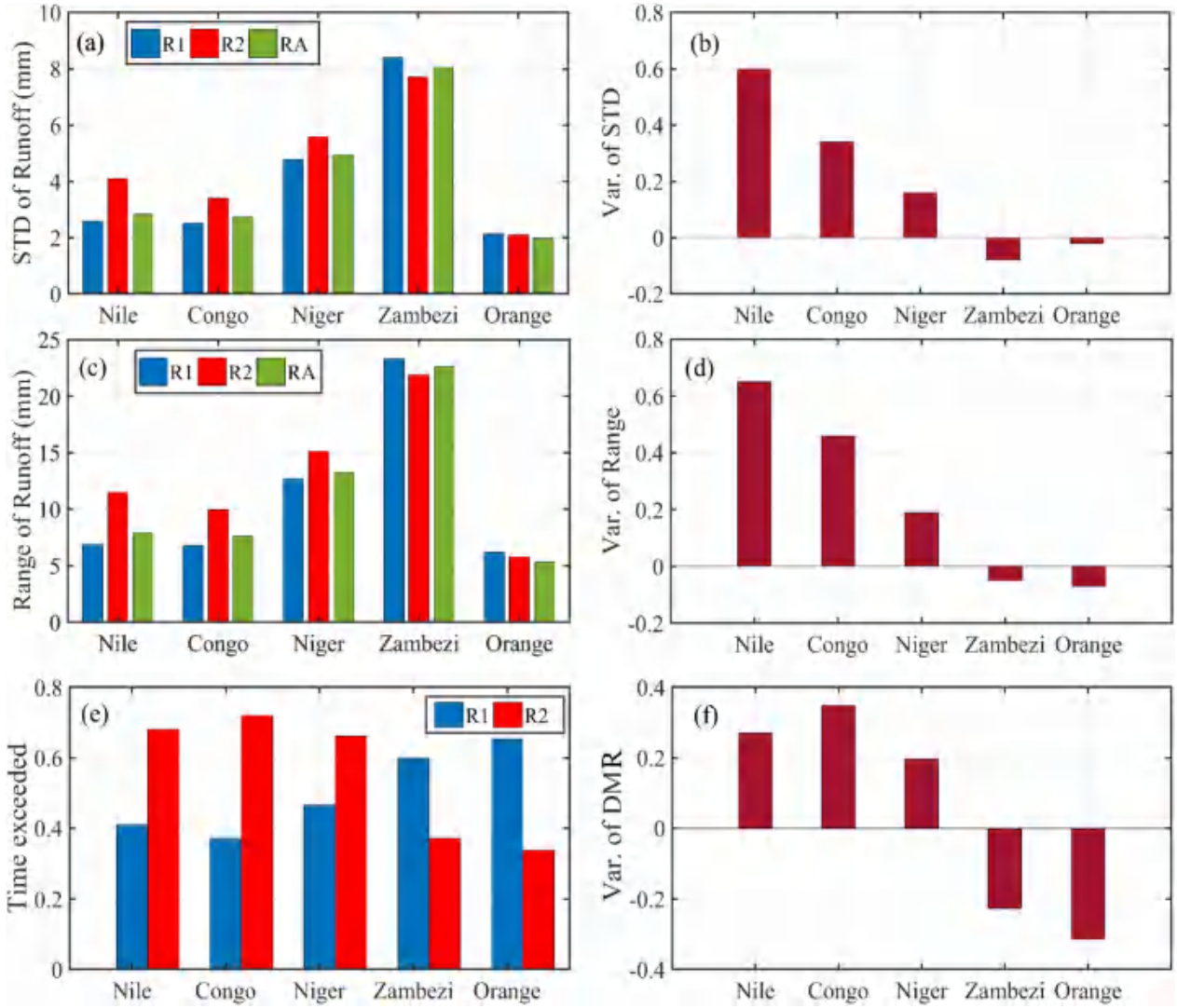

Fig. 17. (a) STD, (c) range (maximum–minimum) of mean monthly runoff, and (e) time exceeding median runoff (DMR) over different periods in the five major basins in Africa. And the relative difference in (b) STD and (d) range, and absolute difference in (f) DMR between R1 and R2.

In the Congo basin [see Fig. 20(c) and (d)], ENSO and runoff indicated a significant antiphase relationship from 2003 to 2010 at a time band of 8–64 months, and from 2003 to 2018, at a time band of 64–96 months. By contrast, IOD and runoff depicted an in-phase relationship from 2003 to 2009, 2003 to 2012, 2012 to 2015, 2014 to 2019, and 2018 to the end of time series, at a time band of 64–96, 32–64, 32–64, 16–32, and 4–16 months, respectively.

Within the Niger basin [see Fig. 20(e) and (f)], ENSO and runoff exhibited an antiphase relationship from 2003 to 2005, at a time band of 4–14 months, and from and 2014 to 2019, at a time band of 32–64 months. In addition, an in-phase relationship between IOD and runoff were traced from 2003 to 2008, at a time band of 64–96, and from 2011 to 2019, at a time band of 32–64 months.

In the Zambezi basin [see Fig. 20(g) and (h)], ENSO and runoff revealed an in-phase relationship from 2003 to 2004, at a time band of 4–16 months, and an antiphase relationship from 2003 to 2019, at a time band of 32–64 months. Likewise, IOD and runoff indicated an in-phase relationships from 2003 to 2007, 2014 to 2019, and 2019 to the end of time series at a time band of 16–64, 32–64, and 16–32 months, respectively.

In the Orange basin [see Fig. 20(i) and (j)], ENSO and runoff demonstrated an antiphase relationship from 2003 to 2011, and 2014 to 2019, at a time band of 16–64 months. Similarly, IOD and runoff exhibited a significant antiphase relationship from 2003 to 2019, at a time band of 16–96 months. Moreover, at a time band of 2–8 months, IOD and runoff illustrated an antiphase and in-phase relationships from 2004 to 2005 and 2006 to 2007, respectively.

The results and analysis indicate that the wavelet coherence method effectively identifies the dynamic relationships between changes in runoff and climate teleconnections. Statistically significant relationships were found between teleconnection factors and runoff changes, demonstrating that these teleconnections play a crucial role in driving alterations in runoff across these basins.

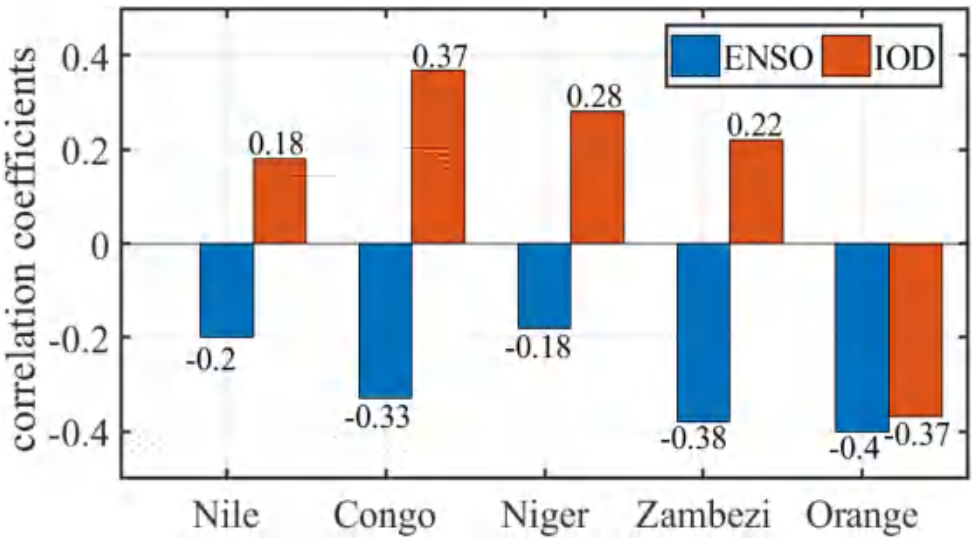

Fig. 18. Correlations between the runoff in five major African's basins and climate teleconnections indices on monthly scale.

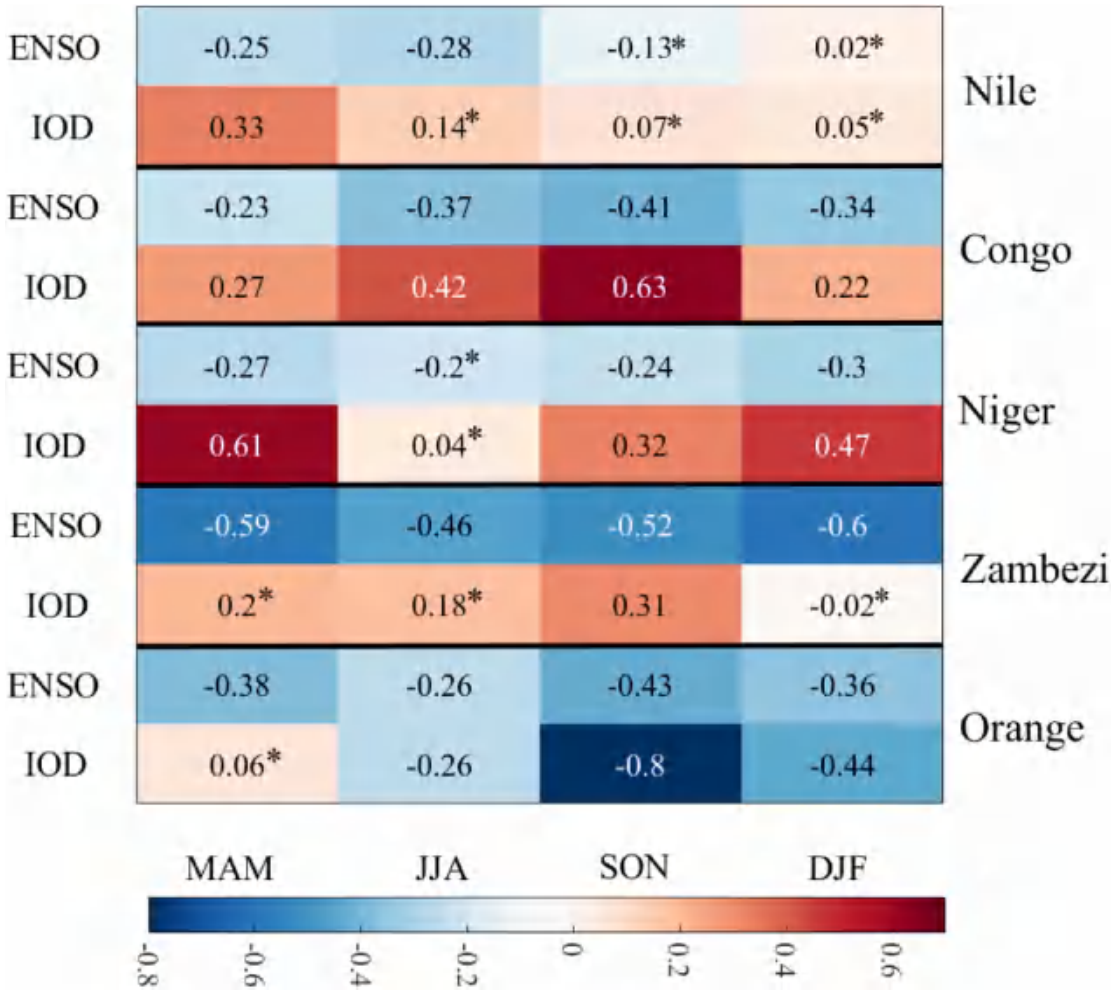

Fig. 19. Seasonal correlations between runoff in five major African's basins and climate teleconnections indices. ∗ indicates that the correlation is nonsignificant at 5% confidence level.

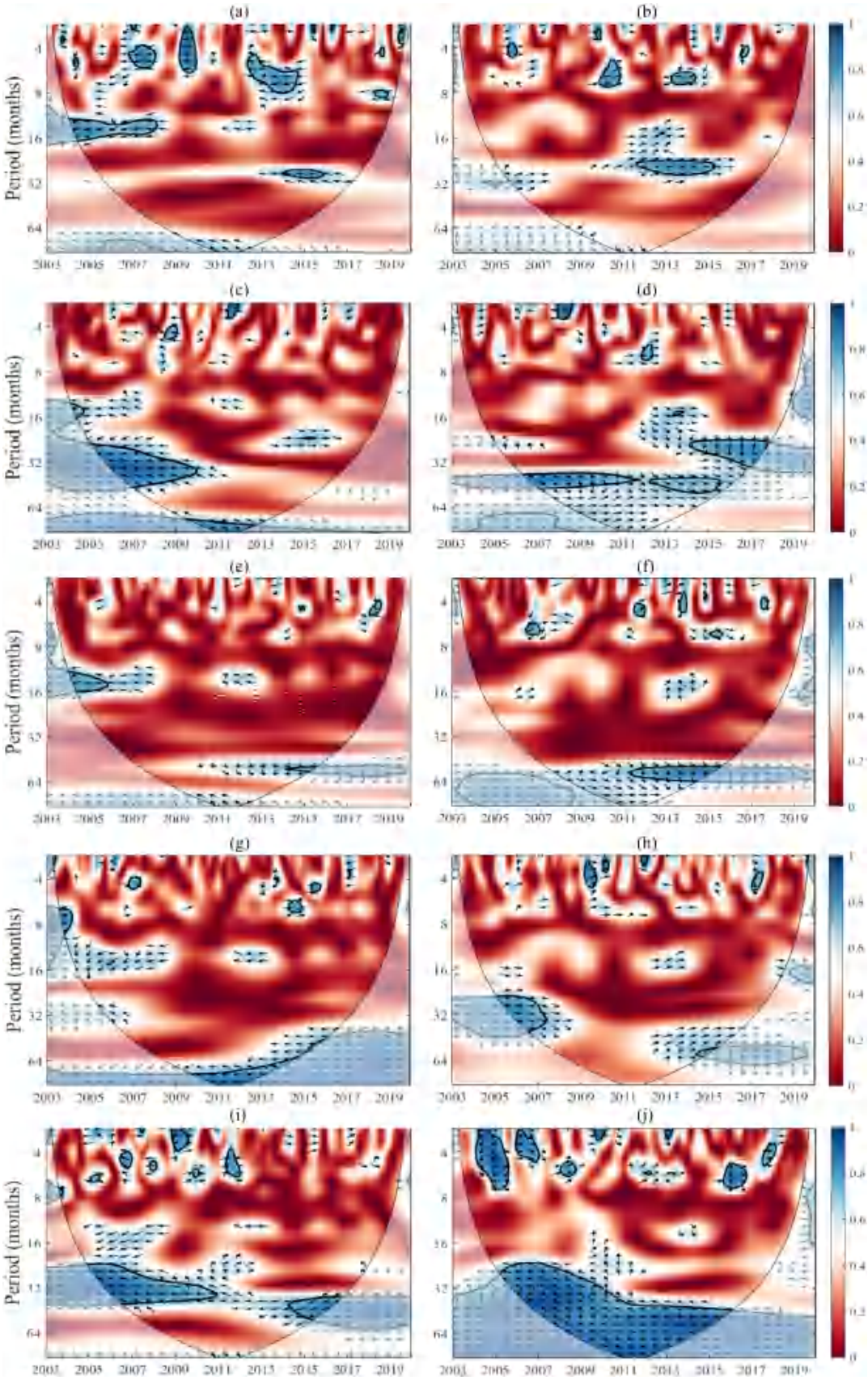

Fig. 20. Wavelet coherence between the runoff in five major African's basins and climate teleconnections indices. (a) Nile: ENSO-Runoff. (b) Nile: IOD-Runoff. (c) Congo: ENSO-Runoff. (d) Congo: IOD-Runoff. (e) Niger: ENSO-Runoff. (f) Niger: IOD-Runoff. (g) Zambezi: ENSO-Runoff. (h) Zambezi: IOD-Runoff. (i) Orange: ENSO-Runoff. (j) Orange: IOD-Runoff.

V. Discussion

GRACE and GRACE-FO satellite observations provide an effective means to monitor large-scale water mass variations, especially in data-scarce regions like Africa. This study estimated monthly runoff time series for Africa's five major basins using GRACE/GRACE-FO-observed water storage, coupled with Prec and ET satellites' datasets for 2003–2019 period based on the water budget framework. We determined a significant consistency among GRACE/GRACE-FO-derived runoff estimates and five runoff products (i.e., GLDAS-NOAH, GLDAS-VIC, GLDAS-CLM, ERA5, and SCS-CN). Findings reported in this study substantiate the applicability and capability of GRACE/GRACE-FO measurements to estimate runoff over the major river basins in Africa. Furthermore, when simulating runoff at larger basin scales, such as the study domain, the GRACE/GRACE-FO model—utilizing remote sensing and water budget methods—offers advantages over process-based models. It requires less parameterization and computational power.

Our analysis shows that climate variability, particularly changes in Prec and Temp, is the main driver of observed runoff trends across the basins. The increasing runoff magnitude in the Nile, Congo, and Niger basins suggests that more runoff contents are being regulated and stringed in these basins. This increased magnitude, combined with increase tended duration, could exacerbate flood hazards in these regions, especially given the heavy rainfall experienced in recent years, such as the floods triggered by massive significant rainfall in some parts of the Nile and Niger basins [143].

The overall rise in runoff variability over the Nile (NRB), Congo (CRB), and Niger (NIRB) basins implies a decline in the stability of their hydrological systems due to ongoing climate dynamics. Greater variability in runoff may also increase the uncertainty and variability of other fluxes such as ET and relative humidity, causing significant obstacles in hydrological forecasting and prediction. The increased runoff variability also suggests that the hydrological system in these basins is becoming more variable. In addition, the accelerated runoff variability indicates that the speed of runoff refresh has also increased, potentially resulting in a more intense hydrological cycle across these basins.

The lower magnitude alongside reduced duration in the Zambezi and Orange basins suggests that while water shortages may be present in both basins, such events are less frequent and occur over longer intervals. This interpretation is supported by Hulsman et al. [144], who analyzed drought conditions in the Zambezi basin from 1992 to 2020 using satellite altimetry and found that drought events occurred at longer intervals. Overall, the reduced duration of runoff change is favorable for water resource management, as it implies less frequent fluctuations in hydrological conditions. Moreover, the lower runoff variability observed in the Zambezi (ZRB) and Orange (ORB) basins suggests a decline in the intensity of hydrological changes, potentially enhancing the stability of water systems in both regions.

Beyond local climate influences, large-scale atmospheric circulations, such as ENSO and IOD, were shown to modulate runoff variability. The correlations between runoff and these teleconnection indices differed significantly between monthly and seasonal scales, indicating that the relationship between atmospheric circulations and runoff is scale dependent. Wavelet coherence analysis further revealed that runoff variability was highly responsive to the oscillations of teleconnection factors (ENSO and IOD).

A negative phase relationship was observed between ENSO and runoff, whereby La Niña events (the cold phase of ENSO) were associated with increased runoff, while El Niño events (the warm phase) led to reduced runoff. This inverse relationship is attributed to the suppression of convection over tropical Africa during El Niño, driven by a weakened Walker Circulation, which reduces Prec and consequently runoff. Conversely, La Niña enhances atmospheric circulation and moisture convergence, thereby increasing runoff [145], [146].

In contrast, a generally positive coherence between the IOD and runoff was observed across the studied basins—except in the Orange basin—implying that warm IOD phases (positive IOD) were associated with increased runoff, while cold phases reduced it. The reversed pattern in the Orange basin, showing negative coherence with the IOD, may reflect region-specific atmospheric responses influenced by its subtropical location and interactions with the South Indian Ocean High [146].

These results underscore the spatially heterogeneous but statistically consistent influence of ocean–atmosphere teleconnections on runoff behavior, shaped by both large-scale and basin-specific dynamics [147], [148]. It is worth mentioning that the mechanism underlying the coherence between global teleconnection oscillations and runoff variability in Africa are much more complex. There are couplings between multiple teleconnection factors, such as North Atlantic Oscillation (NAO), Pacific Decadal Oscillation (PDO), and ENSO. Also, large-scale atmospheric circulations, moisture divergence, anticyclonic circulation, and wind anomalies are coupled together. Therefore, additional studies are required to investigate the effect of these integrated factors on runoff change, for gaining a better understanding of such relationship.

We acknowledge that some shortcomings and uncertainties remain existed in this study. First, the runoff values estimated by GRACE/GRACE-FO showcase some negative values over different basins (see Fig. 17), which can be associated with possible uncertainties in Prec and ET data, as well as the uncertainties included in the estimation of dS/dt. Combining multiple Prec and ET datasets—whether derived from observations or models—along with various GRACE and GRACE-FO solutions can enhance the accuracy of runoff estimations to some extent. However, the overall improvement in these datasets remains contingent upon the development of gauge coverage, which is essential for these basins.

Second, the resolution of GRACE/GRACE-FO measurements has limitations when it comes to analyzing changes in runoff at the subbasin scale or over submonthly periods. Continuous improvements to GRACE/GRACE-FO data processing methods and underlying geophysical models are anticipated, which will enhance the accuracy and resolution of GRACE products in the future.

Third, while the runoff estimates derived from GRACE/GRACE-FO demonstrated a good correlation with various well-established runoff models in this study, it is essential to validate these data using in-situ measurements.

Future research could focus on establishing dense ground station networks in African basins to provide more reliable validation of GRACE/GRACE-FO runoff estimates.

VI. Conclusion

Estimating and monitoring components of the hydrological cycle in regions with limited in-situ data have been enhanced by the use of remote sensing and processing technologies. This study employed observations from the GRACE and GRACE-FO, alongside remotely sensed datasets for Prec and ET, to derive runoff estimates for five major basins in Africa from 2003 to 2019. Two runoff estimates (GRACE-M-R and GRACE-G-R) were generated for each basin, and these results were compared with estimates from GLDAS (using NOAH, CLM, and VIC models), ERA5, and SCS-CN. The mutations of interannual average runoff were identified and the trends were explored. In addition, the study investigated the effects of climatic factors, such as Prec and Temp, on runoff dynamics, focusing on trends and correlations. A comprehensive framework was proposed to quantify both interannual and intraannual runoff regimeswith analyzing their changes in terms of magnitude, variability, and duration. Furthermore, we examined the relationships between global climate teleconnections and runoff using Pearson correlation and wavelet analysis techniques. Main conclusions are summarized as follows:

1) The GRACE/GRACE-FO-derived runoff estimates were in good agreement with those from the GLDAS (NOAH, CLM, and VIC), ERA5, and SCS-CN, as indicated by Pearson's correlation (r) and TSS. Among the five products, the SCS-CN exhibited the highest consistency with the two GRACE/GRACE-FO runoff estimates. GRACE-G-R outperformed GRACE-M-R in representing runoff changes in the studied basins.
2) From 2003 to 2019, runoff in the Nile (0.12–0.46 mm/a, $p < 0.05$) and Congo (0.52–0.76 mm/a, $p < 0.05$) basins was increased across all the seasons, while it was decreased in the Zambezi (–1 to –0.34 mm/a, $p < 0.05$) and Orange (–0.54 to –0.24 mm/a, $p < 0.05$) basins within the same period. The Niger basin depicted a decreasing trend in MAM (–0.1 mm/a), and an increasing trend in JJA (0.04 mm/a), SON (0.27 mm/a), and DJF (0.16 mm/a). The runoff trend experienced a sudden shift around 2010, 2014, 2011, 2011, and 2012 over the Nile, Congo, Niger, Zambezi, and Orange basins, respectively. The magnitude of trend was higher during the postmutation period when compared to the premutation period in the Nile, Congo, and Niger basins, while it was higher during the premutation period than the postmutation period within the Zambezi and Orange basins. Climate change in the study domain remained a significant factor in runoff variations. The Prec and Temp variables were identified as primary factors, contributing to runoff changes, as indicated by their variability and their robust correlation with runoff.
3) Monthly runoff in the Nile, Congo, and Niger basins illustrated a higher positive change in magnitude, accompanied by increased duration and higher variability. Conversely, the Zambezi and Orange basins demonstrated reductions in runoff magnitude, along with lower variability and decreased durations.
4) The large-scale climate teleconnections were found to be associated with runoff change in all basins. The highest connection between ENSO and runoff occurred in JJA across the NRB, SON across the CRB and NIRB, and DJF across the ZRB and ORB. The strongest correlation between the IOD and runoff was observed in MAM for the NRB and NIRB, and in SON for the CRB, ZRB, and ORB. Wavelet coherence analysis demonstrated that the effects of ENSO and IOD on runoff occured simultaneously, as indicated by the significant interannual modes. Notably, high common power variations between these large-scale teleconnection indices and runoff were detected at frequencies ranging from 0.4 to 8 years across the various basins.

The study of this nature can support policymakers and water resource managers in advancing sustainable water management and development strategies. This, in turn, can improve water security, foster long-term resource sustainability, and strengthen climate adaptation measures, thereby enhancing the resilience of these river basins to both present and projected hydroclimatic changes.

References

[1] L. Li et al., "Global trends in water and sediment fluxes of the world's large rivers," *Sci. Bull.*, vol. 65, no. 1, pp. 62–69, 2020, doi: 10.1016/j.scib.2019.09.012.
[2] S. G. Jin, Z. Chen, and H. Peng, "High-frequency centimeter-accuracy water level estimation in the Yangtze River using multi-GNSS interferometric reflectometry," *IEEE Trans. Geosci. Remote Sens.*, vol. 63, 2025, Art. no. 5802713, doi: 10.1109/TGRS.2025.3594071.
[3] L. Yang et al., "Runoff changes in the major river basins of China and their responses to potential driving forces," *J. Hydrol.*, vol. 607, 2022, Art. no. 127536, doi: 10.1016/j.jhydrol.2022.127536.
[4] Y. Zuo, J. Chen, S. Lin, and K. He, "The runoff changes are controlled by combined effects of multiple regional environmental factors in the alpine hilly region of Northwest China," *Sci. Total Environ.*, vol. 862, 2023, Art. no. 160835, doi: 10.1016/j.scitotenv.2022.160835.
[5] S. G. Jin et al., "Remote sensing and its applications using GNSS reflected signals: Advances and prospects," *Satell. Navigat.*, vol. 5, 2024, Art. no. 19, doi: 10.1186/s43020-024-00139-4.
[6] S. Mohanasundaram, M. M. Mekonnen, E. Haacker, C. Ray, S. Lim, and S. Shrestha, "An application of GRACE mission datasets for streamflow and baseflow estimation in the conterminous United States basins," *J. Hydrol.*, vol. 601, 2021, Art. no. 126622, doi: 10.1016/j.jhydrol.2021.126622.
[7] Y. Tramblay et al., "River runoff estimation with satellite rainfall in Morocco," *Hydrol. Sci. J.*, vol. 68, no. 3, pp. 474–487, 2023, doi: 10.1080/02626667.2023.2171295.
[8] H. Fang, P. L. Hrubiak, H. Kato, M. Rodell, W. L. Teng, and B. E. Vollmer, "Global land data assimilation system (GLDAS) products from NASA hydrology data and information services center (HDISC)," in *Proc. ASPRS Annu. Conf.—Bridging Horiz.: New Front. Geospatial Collab.*, 2008, pp. 183–190.
[9] H. M. Schmied et al., "The global water resources and use model WaterGAP v2.2d: Model description and evaluation," *Geosci. Model Develop.*, vol. 14, no. 2, pp. 1037–1079, 2021, doi: 10.5194/gmd-14-1037-2021.
[10] L. Carlee et al., "Famine early warning systems network (FEWS NET) land data assimilation system (LDAS) and other assimilated hydrological data at NASA GES DISC," NASA Goddard space flight center, greenbelt, MD, USA, Rep. GSFC-E-DAA-TN77212, 2020.
[11] F. Zhao et al., "The critical role of the routing scheme in simulating peak river discharge in global hydrological models," *Environ. Res. Lett.*, vol. 12, no. 7, 2017, Art. no. 75003, doi: 10.1088/1748-9326/aa7250.

[12] V. Amiri, S. Ali, and N. Sohrabi, "Estimating the spatio-temporal assessment of GRACE/GRACE-FO derived groundwater storage depletion and validation with in-situ water quality data (Yazd province, central Iran)," *J. Hydrol.*, vol. 620, 2023, Art. no. 129416, doi: 10.1016/j.jhydrol.2023.129416.

[13] S. Hua et al., "Long-term trends in human-induced water storage changes for China detected from GRACE data," *J. Environ. Manage.*, vol. 368, 2024, Art. no. 122253, doi: 10.1016/j.jenvman.2024.122253.

[14] N. Chao et al., "Divergent spatiotemporal variability of terrestrial water storage and eight hydroclimatic components over three different scales of the Yangtze River basin," *Sci. Total Environ.*, vol. 879, 2023, Art. no. 162886, doi: 10.1016/j.scitotenv.2023.162886.

[15] H. Deng, Y. Li, Y. Zhang, and X. Chen, "Monitoring spatio-temporal variations of terrestrial water storage changes and their potential influencing factors in a humid subtropical climate region of Southeast China," *J. Hydrol.*, vol. 634, 2024, Art. no. 131095, doi: 10.1016/j.jhydrol.2024.131095.

[16] B. Khorrami and O. Gündüz, "A holistic overview of the applications of GRACE-observed terrestrial water storage in hydrology and climate science," *Environ. Monit. Assess.*, vol. 197, no. 7, 2025, Art. no. 785, doi: 10.1007/s10661-025-14207-y.

[17] J. Yang et al., "Comparison of groundwater storage changes over losing and gaining aquifers of China using GRACE satellites, modeling and in-situ observations," *Sci. Total Environ.*, vol. 938, 2024, Art. no. 173514, doi: 10.1016/j.scitotenv.2024.173514.

[18] M. Wei, H. Zhou, Z. Luo, and M. Dai, "Tracking inter-annual terrestrial water storage variations over Lake Baikal basin from GRACE and GRACE Follow-On missions," *J. Hydrol.: Regional Stud.*, vol. 40, 2022, Art. no. 101004, doi: 10.1016/j.ejrh.2022.101004.

[19] L. Longuevergne, C. R. Wilson, B. R. Scanlon, and J. F. Crétaux, "GRACE water storage estimates for the middle east and other regions with significant reservoir and lake storage," *Hydrol. Earth Syst. Sci.*, vol. 17, no. 12, pp. 4817–4830, 2013, doi: 10.5194/hess-17-4817-2013.

[20] K. Zhao and X. Li, "Estimating terrestrial water storage changes in the Tarim River Basin using GRACE data," *Geophys. J. Int.*, vol. 211, no. 3, pp. 1449–1460, 2017, doi: 10.1093/GJI/GGX378.

[21] V. Sridhar, S. A. Ali, and V. Lakshmi, "Assessment and validation of total water storage in the Chesapeake Bay watershed using GRACE," *J. Hydrol.: Regional Stud.*, vol. 24, 2019, Art. no. 100607, doi: 10.1016/j.ejrh.2019.100607.

[22] F. Fatolazadeh and K. Goïta, "Mapping terrestrial water storage changes in Canada using GRACE and GRACE-FO," *Sci. Total Environ.*, vol. 779, 2021, Art. no. 146435, doi: 10.1016/j.scitotenv.2021.146435.

[23] A. Tariq et al., "Corrigendum to 'Terrestrial and groundwater storage characteristics and their quantification in the Chitral (Pakistan) and Kabul (Afghanistan) river basins using GRACE/GRACE-FO satellite data' (Groundwater for Sustainable Development (2023) 23, (S2352801X)," *Groundwater Sustain. Develop.*, vol. 23, 2023, Art. no. 100990, doi: 10.1016/j.gsd.2023.101026.

[24] H. A. Mohasseb, W. Shen, J. Jiao, and A. A. Hassan, "Estimation of groundwater storage variations in African river basins: Response to global climate change using GRACE and GRACE-FO among past two decades," *Adv. Space Res.*, vol. 74, no. 3, pp. 1164–1182, 2024, doi: 10.1016/j.asr.2024.05.003.

[25] S. G. Jin and G. Feng, "Large-scale variations of global groundwater from satellite gravimetry and hydrological models, 2002-2012," *Glob. Planet. Change*, vol. 106, pp. 20–30, 2013, doi: 10.1016/j.gloplacha.2013.02.008.

[26] A. M. Elameen, S. Jin, and D. Olago, "Identification of drought events in major basins of Africa from GRACE total water storage and modeled products," *Photogrammetric Eng. Remote Sens.*, vol. 89, no. 4, pp. 221–232, 2023, doi: 10.14358/PERS.22-00092R2.

[27] Z. M. Nigatu, D. Fan, W. You, and A. M. Melesse, "Hydroclimatic extremes evaluation using GRACE/GRACE-FO and multidecadal climatic variables over the Nile River Basin," *Remote Sens.*, vol. 13, no. 4, Feb. 2021, Art. no. 651, doi: 10.3390/rs13040651.

[28] J. Xiong, J. Yin, S. Guo, L. Gu, F. Xiong, and N. Li, "Integrated flood potential index for flood monitoring in the GRACE era," *J. Hydrol.*, vol. 603, 2021, Art. no. 127115, doi: 10.1016/j.jhydrol.2021.127115.

[29] S. Yi and W. Sun, "Evaluation of glacier changes in high-mountain Asia based on 10 year GRACE RL05 models," *J. Geophys. Res. Solid Earth*, vol. 119, no. 3, pp. 2504–2517, 2014, doi: 10.1002/2013JB010860.

[30] S. Yi, Q. Wang, L. Chang, and W. Sun, "Changes in mountain glaciers, lake levels, and snow coverage in the Tianshan monitored by GRACE, ICESat, altimetry, and MODIS," *Remote Sens.*, vol. 8, no. 10, 2016, Art. no. 798, doi: 10.3390/rs8100798.

[31] S. G. Jin, X. Tian, and G. Feng, "Recent glacier changes in the Tien Shan observed by satellite gravity measurements," *Glob. Planet. Change*, vol. 143, pp. 81–87, 2016, doi: 10.1016/j.gloplacha.2016.06.006.

[32] M. He, Z. Li, W. Jiang, Y. Pan, J. Jiao, and Y. Xiao, "Seasonal and interannual fluctuations of glacier mass balance and climate response processes on the Tibetan Plateau based on GRACE/GRACE-FO," *IEEE Trans. Geosci. Remote Sens.*, vol. 61, 2023, Art. no. 4301709, doi: 10.1109/TGRS.2023.3280714.

[33] X. Tian and S. Jin, "Evapotranspiration variations in the Yangtze River Basin from multi-satellite remote sensing data," *J. Water Climate Change*, vol. 11, no. 2, pp. 451–467, 2020, doi: 10.2166/wcc.2018.104.

[34] W. Qu, Z. Jin, Q. Zhang, Y. Gao, P. Zhang, and P. Chen, "Estimation of evapotranspiration in the Yellow River Basin from 2002 to 2020 based on GRACE and GRACE Follow-On observations," *Remote Sens.*, vol. 14, no. 3, 2022, Art. no. 730, doi: 10.3390/rs14030730.

[35] M. Sun et al., "Estimation of actual evapotranspiration in a semiarid region based on grace gravity satellite data—A case study in loess Plateau," *Remote Sens.*, vol. 10, no. 12, 2018, Art. no. 2032, doi: 10.3390/rs10122032.

[36] B. Khorrami, S. Gorjifard, S. Ali, and B. Feizizadeh, "Correction to: Local-scale monitoring of evapotranspiration based on downscaled GRACE observations and remotely sensed data: An application of terrestrial water balance approach (Earth Science Informatics, (2023), 16, 2, (1329-1345), 10.1007/s12145-023-00," *Earth Sci. Informat.*, vol. 16, no. 2, 2023, Art. no. 1947, doi: 10.1007/s12145-023-00989-7.

[37] D. S. Nagale, S. Kannaujiya, P. K. Gautam, A. K. Taloor, and T. Sarkar, "Impact assessment of the seasonal hydrological loading on geodetic movement and seismicity in Nepal Himalaya using GRACE and GNSS measurements," *Geodesy Geodyn.*, vol. 13, no. 5, pp. 445–455, 2022, doi: 10.1016/j.geog.2022.02.006.

[38] S. Swenson, D. Chambers, and J. Wahr, "Estimating geocenter variations from a combination of GRACE and ocean model output," *J. Geophys. Res. Solid Earth*, vol. 113, no. 8, 2008, Art. no. B08410, doi: 10.1029/2007JB005338.

[39] E. Rangelova and M. G. Sideris, "Contributions of terrestrial and GRACE data to the study of the secular geoid changes in North America," *J. Geodyn.*, vol. 46, nos. 3–5, pp. 131–143, 2008, doi: 10.1016/j.jog.2008.03.006.

[40] J. Kostelecký, A. Bezděk, and J. Klokočník, "Global and regional seasonal variations of the geoid detected by GRACE," *Acta Geodyn. Geomater.*, vol. 10, no. 3, pp. 285–291, 2013, doi: 10.13168/AGG.2013.0028.

[41] J. Chen et al., "Basin-scale river runoff estimation from GRACE gravity satellites, climate models, and in situ observations: A case study in the Amazon Basin," *Water Resour. Res.*, vol. 56, no. 10, 2020, Art. no. e2020WR028032, doi: 10.1029/2020WR028032.

[42] W. Rao and W. Sun, "Runoff variations in the Yangtze River Basin and sub-basins based on GRACE, hydrological models, and in-situ data," *Earth Planet. Phys.*, vol. 6, no. 3, pp. 228–240, 2022, doi: 10.26464/epp2022021.

[43] N. Sneeuw et al., "estimating runoff using hydro-geodetic approaches," *Surveys Geophys.*, vol. 35, no. 6, pp. 1333–1359, 2014, doi: 10.1007/s10712-014-9300-4.

[44] B. Duvvuri and E. Beighley, "Estimating monthly river discharges from GRACE/GRACE-FO terrestrial water storage anomalies," *Remote Sens.*, vol. 15, no. 18, 2023, Art. no. 4516, doi: 10.3390/rs15184516.

[45] J. Xie, Y. P. Xu, C. Gao, W. Xuan, and Z. Bai, "Total basin discharge from GRACE and water balance method for the Yarlung Tsangpo River Basin, Southwestern China," *J. Geophys. Res. Atmos.*, vol. 124, no. 14, pp. 7617–7632, 2019, doi: 10.1029/2018JD030025.

[46] Q. Li, B. Zhong, Z. Luo, and C. Yao, "GRACE-based estimates of water discharge over the Yellow River Basin," *Geodesy Geodyn.*, vol. 7, no. 3, pp. 187–193, 2016, doi: 10.1016/j.geog.2016.04.007.

[47] V. G. Ferreira, Z. Gong, X. He, Y. Zhang, and S. A. Andam-Akorful, "Estimating total discharge in the Yangtze River Basin using satellite-based observations," *Remote Sens.*, vol. 5, no. 7, pp. 3415–3430, 2013, doi: 10.3390/rs5073415.

[48] M. Abd-Elbaky and S. Jin, "Estimating runoff in the Nile River Basin from multi-satellite measurements," in *Proc. Int. Conf. Geoinformat.*, 2018, pp. 1–5. doi: 10.1109/GEOINFORMATICS.2018.8557073.

[49] K. Alghafli, A. M. Ali, X. Shi, W. Sloan, A. A. A. Obeid, and M. Shamsudduha, "Evaluation of runoff estimation from GRACE coupled with different meteorological gridded products over the Upper Blue Nile Basin," *J. Hydrol.: Regional Stud.*, vol. 50, 2023, Art. no. 101545, doi: 10.1016/j.ejrh.2023.101545.

[50] G. J. Huffman et al., "The TRMM multisatellite precipitation analysis (TMPA): Quasi-global, multiyear, combined-sensor precipitation estimates at fine scales," *J. Hydrometeorol.*, vol. 8, no. 1, pp. 38–55, Feb. 2007, doi: 10.1175/JHM560.1.

[51] D. Entekhabi et al., "The soil moisture active passive (SMAP) mission," *Proc. IEEE*, vol. 98, no. 5, pp. 704–716, 2010, doi: 10.1109/JPROC.2010.2043918.

[52] R. Allen, A. Irmak, R. Trezza, J. M. H. Hendrickx, W. Bastiaanssen, and J. Kjaersgaard, "Satellite-based ET estimation in agriculture using SEBAL and METRIC," *Hydrol. Process.*, vol. 25, no. 26, pp. 4011–4027, 2011, doi: 10.1002/hyp.8408.

[53] B. D. Tapley et al., "Contributions of GRACE to understanding climate change," *Nat. Climate Change*, vol. 9, no. 5, pp. 358–369, 2019, doi: 10.1038/s41558-019-0456-2.

[54] J. A. Vano, T. Das, and D. P. Lettenmaier, "Hydrologic sensitivities of Colorado River runoff to changes in precipitation and temperature," *J. Hydrometeorol.*, vol. 13, no. 3, pp. 932–949, 2012, doi: 10.1175/JHM-D-11-069.1.

[55] T. G. Gebremicael, Y. A. Mohamed, G. D. Betrie, P. van der Zaag, and E. Teferi, "Trend analysis of runoff and sediment fluxes in the Upper Blue Nile basin: A combined analysis of statistical tests, physically-based models and landuse maps," *J. Hydrol.*, vol. 482, pp. 57–68, 2013, doi: 10.1016/j.jhydrol.2012.12.023.

[56] S. A. Abebe, T. Qin, X. Zhang, and D. Yan, "Wavelet transform-based trend analysis of streamflow and precipitation in Upper Blue Nile River basin," *J. Hydrol.: Regional Stud.*, vol. 44, 2022, Art. no. 101251, doi: 10.1016/j.ejrh.2022.101251.

[57] M. O. Dinka and A. Klik, "Temporal and spatial dynamics of surface run-off from Lake Basaka catchment (Ethiopia) using SCS-CN model coupled with remote sensing and GIS," *Lakes Reserv. Sci. Policy Manag. Sustain. Use*, vol. 25, no. 2, pp. 167–182, 2020, doi: 10.1111/lre.12313.

[58] H. Lee et al., "Characterization of terrestrial water dynamics in the Congo Basin using GRACE and satellite radar altimetry," *Remote Sens. Environ.*, vol. 115, no. 12, pp. 3530–3538, 2011, doi: 10.1016/j.rse.2011.08.015.

[59] D. Alsdorf et al., "Opportunities for hydrologic research in the Congo Basin," *Rev. Geophys.*, vol. 54, no. 2, pp. 378–409, 2016, doi: 10.1002/2016RG000517.

[60] H. C. Jung et al., "Characterization of complex fluvial systems using remote sensing of spatial and temporal water level variations in the Amazon, Congo, and Brahmaputra rivers," *Earth Surf. Process. Landforms*, vol. 35, no. 3, pp. 294–304, 2010, doi: 10.1002/esp.1914.

[61] G. Mahé and J. E. Paturel, "1896-2006 Sahelian annual rainfall variability and runoff increase of Sahelian Rivers," *Comptes Rendus—Geosci.*, vol. 341, no. 7, pp. 538–546, 2009, doi: 10.1016/j.crte.2009.05.002.

[62] E. Efon et al., "Monthly, seasonal, and annual variations of precipitation and runoff over West and Central Africa using remote sensing and climate reanalysis," *Earth Syst. Environ.*, vol. 7, no. 1, pp. 67–82, 2023, doi: 10.1007/s41748-022-00326-w.

[63] V. Aich et al., "Comparing impacts of climate change on streamflow in four large African river basins," *Hydrol. Earth Syst. Sci.*, vol. 18, no. 4, pp. 1305–1321, 2014, doi: 10.5194/hess-18-1305-2014.

[64] R. Beilfuss, D. Moore, C. Bento, and P. Dutton, "Patterns of vegetation change in the Zambezi Delta, Mozambique," Mozambique, Prog. Sustain. Manage. Cahora Bassa Dam Lower Zambezi Valley, Work. Paper 2, 2001.

[65] G. Z. Ndhlovu and Y. E. Woyessa, "Evaluation of streamflow under climate change in the Zambezi river basin of Southern Africa," *Water (Switzerland)*, vol. 13, no. 21, 2021, Art. no. 3114, doi: 10.3390/w13213114.

[66] X. Shi, T. Qin, H. Nie, B. Weng, and S. He, "Changes in major global river discharges directed into the ocean," *Int. J. Environ. Res. Public Health*, vol. 16, no. 8, 2019, Art. no. 1469, doi: 10.3390/ijerph16081469.

[67] R. Q. Grafton et al., "Global insights into water resources, climate change and governance," *Nat. Climate Change*, vol. 3, no. 4, pp. 315–321, 2013, doi: 10.1038/nclimate1746.

[68] M. Achite, T. Caloiero, and A. K. Toubal, "Rainfall and runoff trend analysis in the Wadi Mina Basin (Northern Algeria) using non-parametric tests and the ITA method," *Sustainability*, vol. 14, no. 16, 2022, Art. no. 9892, doi: 10.3390/su14169892.

[69] R. Mahmood and S. Jia, "Assessment of hydro-climatic trends and causes of dramatically declining stream flow to Lake Chad, Africa, using a hydrological approach," *Sci. Total Environ.*, vol. 675, pp. 122–140, 2019, doi: 10.1016/j.scitotenv.2019.04.219.

[70] B. D. Richter, J. V. Baumgartner, J. Powell, and D. P. Braun, "A method for assessing hydrologic alteration within ecosystems," *Conserv. Biol.*, vol. 10, no. 4, pp. 1163–1174, 1996, doi: 10.1046/j.1523-1739.1996.10041163.x.

[71] A. T. Haghighi, H. Marttila, and B. Kløve, "Development of a new index to assess river regime impacts after dam construction," *Glob. Planet. Change*, vol. 122, pp. 186–196, 2014, doi: 10.1016/j.gloplacha.2014.08.019.

[72] T. Cui, F. Tian, T. Yang, J. Wen, and M. Y. A. Khan, "Development of a comprehensive framework for assessing the impacts of climate change and dam construction on flow regimes," *J. Hydrol.*, vol. 590, 2020, Art. no. 125358, doi: 10.1016/j.jhydrol.2020.125358.

[73] K. Stefanidis, Y. Panagopoulos, A. Psomas, and M. Mimikou, "Assessment of the natural flow regime in a Mediterranean river impacted from irrigated agriculture," *Sci. Total Environ.*, vol. 573, pp. 1492–1502, 2016, doi: 10.1016/j.scitotenv.2016.08.046.

[74] A. Kumar, V. K. Tripathi, P. Kumar, and A. Rakshit, "Assessment of hydrologic impact on flow regime due to dam inception using IHA framework," *Environ. Sci. Pollut. Res.*, vol. 30, no. 13, pp. 37821–37844, 2023, doi: 10.1007/s11356-022-24861-1.

[75] W. Guo, X. Jiao, H. Zhou, Y. Zhu, and H. Wang, "Hydrologic regime alteration and influence factors in the Jialing River of the Yangtze River, China," *Sci. Rep.*, vol. 12, no. 1, 2022, Art. no. 11166, doi: 10.1038/s41598-022-15127-4.

[76] H. Mohammed and A. T. Hansen, "Spatial heterogeneity of low flow hydrological alterations in response to climate and land use within the Upper Mississippi River basin," *J. Hydrol.*, vol. 632, 2024, Art. no. 130872, doi: 10.1016/j.jhydrol.2024.130872.

[77] B. Gao, J. Li, and X. Wang, "Analyzing changes in the flow regime of the Yangtze River using the eco-flow metrics and IHA metrics," *Water (Switzerland)*, vol. 10, no. 11, 2018, Art. no. 1552, doi: 10.3390/w10111552.

[78] W. Guo, H. Zhou, X. Jiao, L. Huang, and H. Wang, "Analysis of alterations of the hydrological situation and causes of river runoff in the Min River, China," *Water (Switzerland)*, vol. 14, no. 7, 2022, Art. no. 1093, doi: 10.3390/w14071093.

[79] T. Yang, T. Cui, C. Y. Xu, P. Ciais, and P. Shi, "Development of a new IHA method for impact assessment of climate change on flow regime," *Glob. Planet. Change*, vol. 156, pp. 68–79, 2017, doi: 10.1016/j.gloplacha.2017.07.006.

[80] F. F. Worku, M. Werner, N. Wright, P. Van Der Zaag, and S. S. Demissie, "Flow regime change in an endorheic basin in southern Ethiopia," *Hydrol. Earth Syst. Sci.*, vol. 18, no. 9, pp. 3837–3853, 2014, doi: 10.5194/hess-18-3837-2014.

[81] W. Yang, F. Jin, Y. Si, and Z. Li, "Runoff change controlled by combined effects of multiple environmental factors in a headwater catchment with cold and arid climate in northwest China," *Sci. Total Environ.*, vol. 756, 2021, Art. no. 143995, doi: 10.1016/j.scitotenv.2020.143995.

[82] J. A. Anache, D. C. Flanagan, A. Srivastava, and E. C. Wendland, "Land use and climate change impacts on runoff and soil erosion at the hillslope scale in the Brazilian Cerrado," *Sci. Total Environ.*, vol. 622–623, pp. 140–151, 2018, doi: 10.1016/j.scitotenv.2017.11.257.

[83] M. L. Wine and C. B. Zou, "Long-term streamflow relations with riparian gallery forest expansion into tallgrass prairie in the Southern Great Plains, USA," *Forest Ecol. Manage.*, vol. 266, pp. 170–179, 2012, doi: 10.1016/j.foreco.2011.11.014.

[84] L. T. Tran and R. V. O'Neill, "Detecting the effects of land use/land cover on mean annual streamflow in the Upper Mississippi River Basin, USA," *J. Hydrol.*, vol. 499, pp. 82–90, 2013, doi: 10.1016/j.jhydrol.2013.06.041.

[85] Q. Cheng, X. Zuo, F. Zhong, L. Gao, and S. Xiao, "Runoff variation characteristics, association with large-scale circulation and dominant causes in the Heihe River Basin, Northwest China," *Sci. Total Environ.*, vol. 688, pp. 361–379, 2019, doi: 10.1016/j.scitotenv.2019.05.397.

[86] H. Shiferaw, A. Girma, K. Hadush, H. G. Mariam, E. Yazew, and A. Zenebe, "Long-term hydroclimatic variability over the semi-arid Ethiopian highlands in relation to ENSO and IOD teleconnection signals," *Theor. Appl. Climatol.*, vol. 153, no. 1–2, pp. 193–211, 2023, doi: 10.1007/s00704-023-04450-z.

[87] F. Chauluka, S. Singh, and R. Kumar, "Rainfall and streamflow trends of Thuchila River, Southern Malawi," *Mater. Today: Proc.*, vol. 34, pp. 846–855, 2019, doi: 10.1016/j.matpr.2020.06.228.

[88] P. K. Langat, L. Kumar, and R. Koech, "Temporal variability and trends of rainfall and streamflow in Tana River Basin, Kenya," *Sustainability (Switzerland)*, vol. 9, no. 11, 2017, Art. no. 1963, doi: 10.3390/su9111963.
[89] M. A. Degefu and W. Bewket, "Variability, trends, and teleconnections of stream flows with large-scale climate signals in the Omo-Ghibe River Basin, Ethiopia," *Environ. Monit. Assess.*, vol. 189, no. 4, pp. 1–22, 2017, doi: 10.1007/s10661-017-5862-1.
[90] Z. Li, W. Zhao Liu, X. Chang Zhang, and F. Li Zheng, "Impacts of land use change and climate variability on hydrology in an agricultural catchment on the Loess Plateau of China," *J. Hydrol.*, vol. 377, nos. 1/2, pp. 35–42, 2009, doi: 10.1016/j.jhydrol.2009.08.007.
[91] W. Babiker, G. Tan, M. A. A. Alriah, and A. M. Elameen, "Evaluation and correction analysis of the regional rainfall simulation by CMIP6 over Sudan," *Geogr. Pannonica*, vol. 28, no. 1, pp. 53–70, 2024, doi: 10.5937/gp28-46565.
[92] *Africa Water Atlas*, vol. 1, United Nations Environment Programme: Nairobi, Kenya, 2010, pp. 1–336. [Online]. Available: wedoc.unep.org/20.500.11822/7919
[93] M. Abd-Elbaky and S. Jin, "Hydrological mass variations in the Nile River Basin from GRACE and hydrological models," *Geodesy Geodyn.*, vol. 10, no. 6, pp. 430–438, 2019, doi: 10.1016/j.geog.2019.07.004.
[94] S. Jiang et al., "Utility of integrated IMERG precipitation and GLEAM potential evapotranspiration products for drought monitoring over mainland China," *Atmos. Res.*, vol. 247, Jan. 2021, Art. no. 105141, doi: 10.1016/j.atmosres.2020.105141.
[95] S. Pan et al., "Evaluation of global terrestrial evapotranspiration using state-of-the-art approaches in remote sensing, machine learning and land surface modeling," *Hydrol. Earth Syst. Sci.*, vol. 24, no. 3, pp. 1485–1509, 2020, doi: 10.5194/hess-24-1485-2020.
[96] I. McNamara et al., "How well do gridded precipitation and actual evapotranspiration products represent the key water balance components in the Nile Basin?," *J. Hydrol.: Regional Stud.*, vol. 37, 2021, Art. no. 100884, doi: 10.1016/j.ejrh.2021.100884.
[97] H. Liu, X. Yuan, and M. Zhang, "Unraveling human influence on evapotranspiration over East Asian monsoon river basins by using GRACE/GRACE-FO data and land surface models," *J. Hydrol.*, vol. 605, 2022, Art. no. 127349, doi: 10.1016/j.jhydrol.2021.127349.
[98] H. Hersbach et al., "ERA5 monthly averaged data on pressure levels from 1940 to present," *Copernicus Climate Change Serv. Climate Data Store*, vol. 10, pp. 252–266, 2023. [Online]. Available: https://cds.climate.copernicus.eu/cdsapp#!/dataset/reanalysis-era5-pressure-levels-monthly-means?tab=overview
[99] A. Amazirh, A. Chehbouni, E. H. Bouras, M. Benkirane, B. A. Hssaine, and D. Entekhabi, "Drought cascade lag time estimation across Africa based on remote sensing of hydrological cycle components," *Adv. Water Resour.*, vol. 182, 2023, Art. no. 104586, doi: 10.1016/j.advwatres.2023.104586.
[100] F. Wang et al., "Spatio-temporal evolution and teleconnection factor analysis of groundwater drought based on the GRACE mascon model in the Yellow River Basin," *J. Hydrol.*, vol. 626, 2023, Art. no. 130349, doi: 10.1016/j.jhydrol.2023.130349.
[101] A. M. Al-Abadi, J. A. Al-Mohammdawi, A. K. Abass, F. K. Jabbar, M. S. Mohamod, and H. Alzahrani, "The spatial and temporal variation of the terrestrial water storage anomaly (TWSA) of Iraq for the period 2002–2019 based on GRACE gravity data," *Kuwait J. Sci.*, vol. 51, no. 4, 2024, Art. no. 100275, doi: 10.1016/j.kjs.2024.100275.
[102] Z. Wan, "New refinements and validation of the collection-6 MODIS land-surface temperature/emissivity product," *Remote Sens. Environ.*, vol. 140, no. 1, pp. 36–45, 2014, doi: 10.1016/j.rse.2013.08.027.
[103] N. NourEldeen, K. Mao, Z. Yuan, X. Shen, T. Xu, and Z. Qin, "Analysis of the spatiotemporal change in land surface temperature for a long-term sequence in Africa (2003-2017)," *Remote Sens.*, vol. 12, no. 3, 2020, Art. no. 488, doi: 10.3390/rs12030488.
[104] M. Huang and S. Jin, "Backscatter characteristics analysis for flood mapping using multi-temporal Sentinel-1 images," *Remote Sens.*, vol. 14, no. 15, 2022, Art. no. 3838, doi: 10.3390/rs14153838.
[105] V. K. Rana and T. M. V. Suryanarayana, "GIS-based multi criteria decision making method to identify potential runoff storage zones within watershed," *Ann. GIS*, vol. 26, no. 2, pp. 149–168, 2020, doi: 10.1080/19475683.2020.1733083.
[106] H. H. Jaafar, F. A. Ahmad, and N. El Beyrouthy, "GCN250, new global gridded curve numbers for hydrologic modeling and design," *Sci. Data*, vol. 6, no. 1, 2019, Art. no. 145, doi: 10.1038/s41597-019-0155-x.
[107] J. Wahr, M. Molenaar, and F. Bryan, "Time variability of the Earth's gravity field: Hydrological and oceanic effects and their possible detection using GRACE," *J. Geophys. Res. Solid Earth*, vol. 103, no. B12, pp. 30205–30229, 1998, doi: 10.1029/98jb02844.
[108] Y. Sun, R. Riva, and P. Ditmar, "Optimizing estimates of annual variations and trends in geocenter motion and J2 from a combination of GRACE data and geophysical models," *J. Geophys. Res. Solid Earth*, vol. 121, no. 11, pp. 8352–8370, 2016, doi: 10.1002/2016JB013073.
[109] S. Jin, L. J. Zhang, and B. D. Tapley, "The understanding of length-of-day variations from satellite gravity and laser ranging measurements," *Geophys. J. Int.*, vol. 184, no. 2, pp. 651–660, 2011, doi: 10.1111/j.1365-246X.2010.04869.x.
[110] W. R. Peltier, D. F. Argus, and R. Drummond, "Comment on 'An assessment of the ICE-6G_C (VM5a) glacial isostatic adjustment model' by Purcell et al.," *J. Geophys. Res. Solid Earth*, vol. 123, no. 2, pp. 2019–2028, 2018, doi: 10.1002/2016JB013844.
[111] F. W. Landerer and S. C. Swenson, "Accuracy of scaled GRACE terrestrial water storage estimates," *Water Resour. Res.*, vol. 48, no. 4, 2012, Art. no. W04531, doi: 10.1029/2011WR011453.
[112] S. Swenson and J. Wahr, "Post-processing removal of correlated errors in GRACE data," *Geophys. Res. Lett.*, vol. 33, no. 8, 2006, Art. no. L08402, doi: 10.1029/2005GL025285.
[113] M. Khaki, E. Forootan, M. Kuhn, J. Awange, L. Longuevergne, and Y. Wada, "Efficient basin scale filtering of GRACE satellite products," *Remote Sens. Environ.*, vol. 204, pp. 76–93, 2018, doi: 10.1016/j.rse.2017.10.040.
[114] A. M. Seka, J. Zhang, G. T. Ayele, Y. G. Demeke, J. Han, and F. A. Prodhan, "Spatio-temporal analysis of water storage variation and temporal correlations in the East Africa lake basins," *J. Hydrol.: Regional Stud.*, vol. 41, 2022, Art. no. 101094, doi: 10.1016/j.ejrh.2022.101094.
[115] R. K. Sahu, S. K. Mishra, and T. I. Eldho, "Comparative evaluation of SCS-CN-inspired models in applications to classified datasets," *Agric. Water Manage.*, vol. 97, no. 5, pp. 749–756, 2010, doi: 10.1016/j.agwat.2010.01.005.
[116] D. Uwizeyimana, S. M. Mureithi, S. M. Mvuyekure, G. Karuku, and G. Kironchi, "Modelling surface runoff using the soil conservation service-curve number method in a drought prone agro-ecological zone in Rwanda," *Int. Soil Water Conserv. Res.*, vol. 7, no. 1, pp. 9–17, 2019, doi: 10.1016/j.iswcr.2018.12.001.
[117] R. B. Cleveland, W. S. Cleveland, J. E. McRae, and I. Terpenning, "STL: A seasonal-trend decomposition," *J. Official Statist.*, vol. 6, no. 1, pp. 3–73, 1990.
[118] A. N. Pettitt, "A non-parametric approach to the change-point problem," *J. Roy. Stat. Soc., Ser. C (Appl. Statist.)*, vol. 28, no. 2, pp. 126–135, 1979.
[119] L. Wang, J. Wang, L. Wang, L. Zhu, and X. Li, "Terrestrial water storage regime and its change in the endorheic Tibetan Plateau," *Sci. Total Environ.*, vol. 815, 2022, Art. no. 152729, doi: 10.1016/j.scitotenv.2021.152729.
[120] L. Wang, J. Wang, M. Li, L. Wang, X. Li, and L. Zhu, "Response of terrestrial water storage and its change to climate change in the endorheic Tibetan Plateau," *J. Hydrol.*, vol. 612, 2022, Art. no. 128231.
[121] A. Hussain et al., "Ocean-atmosphere circulation coherences associated with temperature increase in Pakistan," *Environ. Res. Lett.*, vol. 18, no. 9, 2023, Art. no. 94028, doi: 10.1088/1748-9326/acee99.
[122] A. S. Al-Sakkaf et al., "Assessing exposure to climate extremes over the Arabian Peninsula using ERA5 reanalysis data: Spatial distribution and temporal trends," *Atmos. Res.*, vol. 300, 2024, Art. no. 107224, doi: 10.1016/j.atmosres.2024.107224.
[123] M. S. Nashwan, S. Shahid, and N. A. Rahim, "Unidirectional trends in annual and seasonal climate and extremes in Egypt," *Theor. Appl. Climatol.*, vol. 136, no. 1–2, pp. 457–473, 2019, doi: 10.1007/s00704-018-2498-1.
[124] S. Yue and C. Y. Wang, "The Mann-Kendall test modified by effective sample size to detect trend in serially correlated hydrological series," *Water Resour. Manage.*, vol. 18, no. 3, pp. 201–218, 2004, doi: 10.1023/B:WARM.0000043140.61082.60.
[125] K. G. Berhanu, T. K. Lohani, and S. D. Hatiye, "Comparative evaluation of the dynamics of terrestrial water storage and drought incidences using multiple data sources: Tana sub-basin, Ethiopia," *J. Water Climate Change*, vol. 15, no. 3, pp. 1102–1119, 2024.
[126] M. M. Monir, S. C. Sarker, S. K. Sarkar, M. Ahmed, J. Mallick, and A. R. M. T. Islam, "Groundwater level fluctuations and associated influencing factors in Rangpur District, Bangladesh, using modified Mann-Kendall and GIS-based AHP technique," *Theor. Appl. Climatol.*, vol. 153, nos. 3/4, pp. 1323–1339, 2023, doi: 10.1007/s00704-023-04541-x.

[127] H. Babaousmail et al., "Evaluation of the performance of cmip6 models in reproducing rainfall patterns over North Africa," *Atmos. (Basel)*, vol. 12, no. 4, 2021, Art. no. 475, doi: 10.3390/atmos12040475.
[128] M. Fan et al., "Recent Tianshan warming in relation to large-scale climate teleconnections," *Sci. Total Environ.*, vol. 856, 2023, Art. no. 159201, doi: 10.1016/j.scitotenv.2022.159201.
[129] A. Hussain et al., "Wavelet coherence of monsoon and large-scale climate variabilities with precipitation in Pakistan," *Int. J. Climatol.*, vol. 42, no. 16, pp. 9950–9966, 2022, doi: 10.1002/joc.7874.
[130] K. S. Kumar, P. Anandraj, K. Sreelatha, D. S. Bisht, and V. Sridhar, "Monthly and seasonal drought characterization using grace-based groundwater drought index and its link to teleconnections across south Indian river basins," *Climate*, vol. 9, no. 4, 2021, Art. no. 56, doi: 10.3390/cli9040056.
[131] M. W. Burnett, G. R. Quetin, and A. G. Konings, "Data-driven estimates of evapotranspiration and its controls in the Congo Basin," *Hydrol. Earth Syst. Sci.*, vol. 24, no. 8, pp. 4189–4211, 2020, doi: 10.5194/hess-24-4189-2020.
[132] S. Bibi et al., "Effects of climate change on terrestrial water storage and basin discharge in the Lancang River Basin," *J. Hydrol.: Regional Stud.*, vol. 37, 2021, Art. no. 100896, doi: 10.1016/j.ejrh.2021.100896.
[133] H. Deng, N. C. Pepin, Q. Liu, and Y. Chen, "Understanding the spatial differences in terrestrial water storage variations in the Tibetan Plateau from 2002 to 2016," *Climate Change*, vol. 151, nos. 3/4, pp. 379–393, 2018, doi: 10.1007/s10584-018-2325-9.
[134] M. Lv, Z. Ma, M. Li, and Z. Zheng, "Quantitative analysis of terrestrial water storage changes under the grain for green program in the Yellow River Basin," *J. Geophys. Res. Atmos.*, vol. 124, no. 3, pp. 1336–1351, 2019, doi: 10.1029/2018JD029113.
[135] M. Sidibe et al., "Near-term impacts of climate variability and change on hydrological systems in West and Central Africa," *Climate Dyn.*, vol. 54, nos. 3/4, pp. 2041–2070, 2020, doi: 10.1007/s00382-019-05102-7.
[136] D. G. Miralles et al., "The WACMOS-ET project - Part 2: Evaluation of global terrestrial evaporation data sets," *Hydrol. Earth Syst. Sci.*, vol. 20, no. 2, pp. 823–842, 2016, doi: 10.5194/hess-20-823-2016.
[137] N. Alahacoon, M. Edirisinghe, M. Simwanda, E. N. C. Perera, V. R. Nyirenda, and M. Ranagalage, "Rainfall variability and trends over the African continent using TAMSAT data (1983–2020): Towards climate change resilience and adaptation," *Remote Sens.*, vol. 14, no. 1, 2022, Art. no. 96, doi: 10.3390/rs14010096.
[138] C. Nhemachena et al., "Climate change impacts on water and agriculture sectors in southern Africa: Threats and opportunities for sustainable development," *Water (Switzerland)*, vol. 12, no. 10, pp. 1–17, 2020, doi: 10.3390/w12102673.
[139] C. B. Chisanga et al., "Modelling climatic trends for the Zambezi and Orange River Basins: Implications on water security," *J. Water Climate Change*, vol. 13, no. 3, pp. 1275–1296, 2022, doi: 10.2166/wcc.2022.308.
[140] C. Munday and R. Washington, "Controls on the diversity in climate model projections of early summer drying over southern Africa," *J. Climate*, vol. 32, no. 12, pp. 3707–3725, 2019, doi: 10.1175/JCLI-D-18-0463.1.
[141] S. K. Mgquba and S. Majozi, "Climate change and its impacts on hydropolitics in transboundary basins: A case study of the Orange-Senqu river basin," *J. Water Climate Change*, vol. 11, no. 1, pp. 150–165, 2020, doi: 10.2166/wcc.2018.166.
[142] B. R. Scanlon et al., "Linkages between GRACE water storage, hydrologic extremes, and climate teleconnections in major African aquifers," *Environ. Res. Lett.*, vol. 17, no. 1, 2022, Art. no. 14046.
[143] N. A. Elagib, I. S. Al Zayed, S. A. G. Saad, M. I. Mahmood, M. Basheer, and A. H. Fink, "Debilitating floods in the Sahel are becoming frequent," *J. Hydrol.*, vol. 599, 2021, Art. no. 126362.
[144] P. Hulsman, H. H. G. Savenije, and M. Hrachowitz, "Satellite-based drought analysis in the Zambezi River Basin: Was the 2019 drought the most extreme in several decades as locally perceived?," *J. Hydrol.: Regional Stud.*, vol. 34, 2021, Art. no. 100789.
[145] K. E. Trenberth, G. W. Branstator, D. Karoly, A. Kumar, N. Lau, and C. Ropelewski, "Progress during TOGA in understanding and modeling global teleconnections associated with tropical sea surface temperatures," *J. Geophys. Res. Ocean.*, vol. 103, no. C7, pp. 14291–14324, 1998.
[146] P. Driver and C. J. C. Reason, "Variability in the Botswana High and its relationships with rainfall and temperature characteristics over southern Africa," *Int. J. Climatol.*, vol. 37, pp. 570–581, 2017.
[147] N. H. Saji, B. N. Goswami, P. N. Vinayachandran, and T. Yamagata, "A dipole mode in the tropical Indian Ocean," *Nature*, vol. 401, no. 6751, pp. 360–363, 1999.
[148] S. K. Behera and T. Yamagata, "Influence of the Indian Ocean dipole on the Southern Oscillation," *J. Meteorol. Soc. Jpn. Ser. II*, vol. 81, no. 1, pp. 169–177, 2003.

Ayman M. Elameen received the B.Eng. (Hons.) degree in surveying engineering from the Sudan University of Science and Technology, Khartoum, Sudan, in 2015, the M.Eng. degree in geodesy and engineering surveying from Hohai University, Nanjing, China, in 2018, and the Ph.D. degree in remote sensing and geomatics engineering from the Nanjing University of Information Science and Technology, Nanjing, in 2025.

His research interests include space geodesy, remote sensing, hydrology, and climate change.

Shuanggen Jin (Senior Member, IEEE) was born in Anhui, China, in September 1974. He received the B.Sc. degree in geodesy from Wuhan University, Wuhan, China, in 1999, and the Ph.D. degree in geodesy from the University of Chinese Academy of Sciences, Beijing, China, in 2003.

He is currently the Vice-President and Professor with Henan Polytechnic University, Jiaozuo, China. He has authored or coauthored more than 500 papers in peer-reviewed journals and proceedings, 30 patents/software copyrights, and 15 books/monographs with more than 17 000 citations and H-index >70. His main research interests include satellite navigation, remote sensing, and space/planetary exploration.

Prof. Jin was the recipient of the 100-Talent Program of the Chinese Academy of Sciences and Leading Talent of Ten-Thousand Talents Program, China. He was the President of the International Association of Planetary Sciences from 2015 to 2019, the President of the International Association of Chinese Professionals in GNSS (CPGNSS) from 2016 to 2017, the Chair of the International Union of Geodesy and Geophysics Union Commission on Planetary Sciences (IUGG UCPS) from 2015 to 2027, the Editor-in-Chief for *International Journal of Geosciences*, an Editor for *Geoscience Letters*, an Associate Editor for IEEE TRANSACTIONS ON GEOSCIENCE AND REMOTE SENSING and *Journal of Navigation*, and an Editorial Board Member for *GPS Solutions* and *Journal of Geodynamics*. He was a Fellow of the International Association of Geodesy, the International Union of Geodesy and Geophysics, and the Electromagnetics Academy, a World Class Professor of the Ministry of Education and Cultures (Indonesia), the Chief Scientist of the National Key R&D Program (China), and a Member of the National Academy of Artificial Intelligence (USA), the Russian Academy of Natural Sciences, the European Academy of Sciences, the Turkish Academy of Sciences, and Academia Europaea.

Isaac Sarfo received the B.Sc. degree in environment and development studies from Central University, Accra, Ghana, in 2014, the M.Sc. degree in marine ecosystem management and climate change from Nha Trang University, Nha Trang, Vietnam, and the University of Tromsø, Tromsø, Norway, in 2018, and the Ph.D. degree in history of science and technology from the Nanjing University of Information Science and Technology, Nanjing, China, in 2023.

Dr. Sarfo is currently a Research Fellow with the College of Geography and Environmental Science, Henan University, Kaifeng, China. His research interests include urban development, regional planning, geographic information system and remote sensing, sustainable development, and land governance.